IRIS AperTO

UNIVERSITÀ DEGLI STUDI DI TORINO

AperTO - Archivio Istituzionale Open Access dell'Università di Torino

Partial melting due to breakdown of an epidote-group mineral during exhumation of ultrahigh-pressure eclogite: An example from the North-East Greenland Caledonides

This is a pre print version of the following article:

Original Citation:

Availability:

This version is available http://hdl.handle.net/2318/1691542 since 2019-02-10T16:14:23Z

Published version:

DOI:10.1111/jmg.12447

Terms of use:

Open Access

Anyone can freely access the full text of works made available as "Open Access". Works made available under a Creative Commons license can be used according to the terms and conditions of said license. Use of all other works requires consent of the right holder (author or publisher) if not exempted from copyright protection by the applicable law.

(Article begins on next page)

30 May 2024

Accepted Article

Partial melting due to breakdown of an epidote-group mineral during exhumation of ultrahigh-pressure eclogite: an example from the North-East Greenland Caledonides

Wentao Cao[1, *], Jane A. Gilotti[1], Hans-Joachim Massonne[2], Simona Ferrando[3], C. Thomas Foster,[1]
[1]Department of Earth & Environmental Sciences, 115 Trowbridge Hall, University of Iowa, Iowa City, IA 52242, USA
[2]Institut für Mineralogie und Kristallchemie, Azenbergstraße 18, Universität Stuttgart, D-70174, Stuttgart, Germany
[3]Department of Earth Sciences, University of Torino, Via Valperga Caluso 35, Torino 10125, Italy

*Corresponding author, current address:
Wentao Cao
205 Jewett Hall, Department of Geology and Environmental Sciences,
State University of New York at Fredonia
Fredonia, NY 14063
U.S.A.
Email: cao@fredonia.edu

Short title: Partial melting of Greenland UHP eclogite

ABSTRACT

In the North-East Greenland Caledonides, *P–T* conditions and textures are consistent with partial melting of UHP eclogite during exhumation. The eclogite contains a peak assemblage of garnet, omphacite, kyanite, coesite, rutile and clinozoisite; in addition, phengite is inferred to have been present at peak conditions. An isochemical phase equilibrium diagram, along with garnet isopleths, constrains peak *P–T* conditions to be subsolidus at 3.4 GPa and 940 ˚C. Zr-in-rutile thermometry on inclusions in garnet yields values around 820 ˚C at 3.4 GPa. In the eclogite, plagioclase may exhibit cuspate textures against surrounding omphacite and has low dihedral angles in plagioclase–clinopyroxene–garnet aggregates, features that are consistent with former melt–solid–solid boundaries and crystallized melt pockets. Graphic intergrowths of plagioclase and amphibole are present in the matrix. Small euhedral neoblasts of garnet against plagioclase are interpreted as formed from a peritectic reaction during partial melting. Polymineralic inclusions of albite+K-feldspar and clinopyroxene+quartz±kyanite±plagioclase in large anhedral garnet display plagioclase cusps pointing into the host, which are interpreted as crystallized melt pockets. These textures, along with the mineral composition, suggest partial melting of the eclogite by reactions involving phengite and, to a large extent, an epidote-group mineral. Calculated and experimentally determined phase relations from the literature reveal that partial melting occurred on the exhumation path, at pressures below the coesite to quartz transition. A calculated *P–T* phase diagram for a former melt-bearing domain shows that the formation of the peritectic garnet rim occurred at 1.4 GPa and 900 ˚C, with an assemblage of clinopyroxene, amphibole and plagioclase equilibrated at 1.3 GPa and 720 ˚C. Isochemical phase equilibrium modelling of a symplectite of clinopyroxene, plagioclase and amphibole

This article has been accepted for publication and undergone full peer review but has not been through the copyediting, typesetting, pagination and proofreading process, which may lead to differences between this version and the Version of Record. Please cite this article as doi: 10.1111/jmg.12447
This article is protected by copyright. All rights reserved.

after omphacite, combined with the mineral composition, yields a *P–T* range at 1.0–1. 6 GPa, 680–1000 ˚C. The assemblage of amphibole and plagioclase is estimated to reach equilibrium at 717–732 ˚C, calculated by amphibole-plagioclase thermometry for the former melt-bearing domain and symplectite, respectively. The results of this study demonstrate that partial melt formed in the UHP eclogite through breakdown of an epidote-group mineral with minor involvement of phengite during exhumation from peak pressure; melt was subsequently crystallized on the cooling path.

KEYWORDS:
Eclogite melting, melt-related textures, phase equilibria, North-East Greenland Caledonides, UHP metamorphism.

1 | INTRODUCTION

Partial melting of HP and UHP eclogite is a fundamental process leading to crustal differentiation, crust-mantle interaction and mantle metasomatism, and may have a considerable influence on large-scale tectonics (e.g. Hermann & Rubatto, 2014; Zheng, Xia, Chen, & Gao, 2011). The key factors controlling partial melting are fluid, pressure, temperature and bulk composition, influences which have been explored by numerous experimental studies (Massonne & Fockenberg, 2015; Schmidt & Poli, 2014 and references therein). Because free fluid is limited at deep crustal to upper mantle depth, melting due to breakdown of hydrous minerals (i.e. phengite and zoisite) is the most plausible way to partially melt eclogite (Hermann & Rubatto, 2014; Schmidt & Poli, 2014; Zheng et al., 2011). Experiments on basaltic rocks show that the composition of partial melt tends to be granitic, tonalitic, trondhjemitic or granodioritic, depending on physical conditions, source materials and degree of partial melting (e.g. Q. Liu, Jin, & Zhang, 2009; Rapp & Watson, 1995; Rapp, Watson, & Miller, 1991; Skjerlie & Patiño Douce, 2002). Discrepancies still exist for phase boundaries of hydrous minerals with respect to solidus conditions in *P–T* space (Q. Liu et al., 2009; Rapp & Watson, 1995; Schmidt, Vielzeuf, & Auzanneau, 2004; Skjerlie & Patiño Douce, 2002; Vielzeuf & Schmidt, 2001). Petrological studies on partial melting of natural UHP eclogite are few (Y. X. Chen, Zheng, Gao, & Hu, 2014; Gao, Zheng, & Chen, 2012; Gao, Zheng, Chen, & Hu, 2014; Hacker et al., 2005; L. Wang et al., 2014), partly due to limited field occurrence of UHP eclogite with preserved evidence of melting in the textures, which are easily destroyed. Melt may connect and channelize, forming felsic veins or networks on the mesoscale, and segregate, leading to melt escape from the source area (e.g. Brown, 2007; Kriegsman, 2001; Rosenberg & Handy, 2005; Sawyer, 2001) contributing to relamination of subducted materials (Hacker, Kelemen, & Behn, 2011).

Documenting partial melting textures of UHP eclogite on both meso- and micro-scales is critical for understanding anatexis of metabasite. On the outcrop scale, felsic veins, irregular patches and lenses of granitic (Gilotti, McClelland, & Wooden, 2014; F. L. Liu, Robinson, & Liu, 2012; McClelland, Gilotti, Mazdab, & Wooden, 2009; S. J. Wang et al., 2017; Zhao, Zheng, Wei, & Wu, 2007), dacitic (L. Wang et al., 2014), tonalitic (D. L. Chen, Liu, Sun, & Zhu, 2010) and trondhjemitic composition (Labrousse, Prouteau, & Ganzhorn, 2011; Shatsky et al., 1999) have been interpreted as crystallized melt derived from eclogite. Geochemical characteristics of the melt composition may aid interpretation of the melting process; for example, the depletion of heavy rare earth elements (HREE) is a feature of trondhjemite veins in eclogite and is attributed to partial melting in the presence of garnet (Shatsky et al., 1999). On the micro-scale, UHP eclogite may contain features, such as cusps, graphic intergrowths, inclusions of melt and triple junctions among equant minerals (e.g.

This article is protected by copyright. All rights reserved.

Accepted Article

Fenn, 1986; Holness, Cesare, & Sawyer, 2011; Holness & Sawyer, 2008; Sawyer, 2001), among which the inclusions of melt are most commonly used to decipher partial melting of metabasites. Inclusions of K-feldspar+quartz±plagioclase±albite± calcite±barite in garnet, omphacite and clinopyroxene in UHP eclogite from the Sulu-Dabie and Kokchetav areas are interpreted as crystallized melt (Y. X. Chen et al., 2014; Gao et al., 2014; Hwang et al., 2005; L. Wang et al., 2014). Partial melting of eclogite is inferred to be due to the breakdown of hydrous minerals, phengite (Gao et al., 2014; Q. Liu, Hermann, & Zhang, 2013; L. Wang et al., 2014; Zeng, Liang, Asimow, Chen, & Chen, 2009), or phengite, paragonite, and zoisite (Y. X. Chen et al., 2014) on the retrograde path.

In this contribution, we report the results of a study on UHP kyanite eclogite from the North-East Greenland Caledonides. Partial melting textures are documented on the micro-scale, and *P–T* conditions of peak metamorphism, partial melting and melt crystallization are estimated utilizing petrographic observation, phase equilibrium modelling, empirical thermobarometry and Zr-in-rutile thermometry. Petrographic textures, such as inclusions of crystallized melt, cuspate boundaries, graphic intergrowths and euhedral crystals, are interpreted as inherited from melt crystallization. Mineralogy and composition of mm-sized crystallized melt pockets suggest that an epidote-group mineral is the major phase that contributed to partial melting. Experimental phase relations and phase equilibrium modelling show that melting and subsequent crystallization occurred on the exhumation path.

2 | GEOLOGICAL SETTING

The North-East Greenland Eclogite Province (NEGEP) is located on the northeast margin of Laurentia, which was the overriding plate during the Caledonian collision with Baltica (Gilotti & McClelland, 2007). The NEGEP (Figure 1) covers an area of ~ 50,000 km^2 from latitude 76° to 80°30' N and constitutes the uppermost thrust sheet in the North-East Greenland Caledonides (Gilotti, Jones, & Elvevold, 2008). Vast areas of quartzofeldspathic gneiss with eclogitic blocks and rare metapelite (Gilotti, 1993) are exposed in the NEGEP. The eclogitic rocks include eclogites *senso stricto,* garnet clinopyroxenites, garnet websterites, websterites and coronitic metagabbros (Gilotti et al., 2008). Protoliths of the gneisses are Paleoproterozoic granodioritic rocks derived from 2.0–1.8 Ga calc-alkaline batholiths that were intruded by anorogenic granites at 1.75 Ga (Kalsbeek et al., 2008). Protoliths of the mafic and ultramafic rocks were inferred to be mafic xenoliths in the Paleoproterozoic batholiths, dykes and layered intrusions (Gilotti, 1993). Using the garnet-clinopyroxene Fe-Mg exchange thermometer (Ellis & Green, 1979), two pyroxene thermometry (Brey & Köhler, 1990), garnet-orthopyroxene and Al-in-pyroxene barometry (Brey & Köhler, 1990; Harley & Green, 1982), peak *P–T* conditions for the HP mafic rocks were estimated to be 1.8 to 2.35 GPa, 750–850 ºC (Brueckner, Gilotti, & Nutman, 1998; Elvevold & Gilotti, 2000). Widespread HP metamorphism occurred between 425 and 390 Ma based on Sm–Nd mineral isochrons and U–Pb dating of zircon (Gilotti, Nutman, & Brueckner, 2004; Hallett, McClelland, & Gilotti, 2014; McClelland, Gilotti, Ramarao, Stemmerik, & Dalhoff, 2016). The HP metamorphism is formed by overthickening crust in the upper plate due to the Caledonian collision between Laurentia and Baltica (Gilotti & McClelland, 2007).

Local UHP metamorphism, indicated by coesite-bearing zircon in both gneiss and eclogite, has been identified in the easternmost NEGEP on a small island, informally called Rabbit Ears Island (Gilotti & Ravna, 2002; McClelland, Power, Gilotti, & Mazdab, 2006). The UHP terrane is composed of the same Paleoproterozoic quartzofeldspathic gneiss with enclaves of eclogite as seen in the larger NEGEP. Whole rock and trace element geochemistry and U–Pb ages of zircon rims demonstrate that the gneiss has the same Laurentian protolith as the HP terrane (Gilotti & McClelland, 2011). UHP kyanite eclogite consists of garnet+omphacite+ kyanite+coesite+phengite+rutile+zircon±amphibole with

This article is protected by copyright. All rights reserved.

symplectite after omphacite. Peak *P–T* conditions were estimated to be 3.6 GPa and 970 °C (Gilotti & Ravna, 2002) using empirical garnet-clinopyroxene-kyanite-phengite-coesite thermobarometry (Ravna & Terry, 2004). The age of the UHP metamorphism is 365–350 Ma based on U–Pb ion probe dating of coesite-bearing zircon domains (Gilotti et al., 2014; McClelland et al., 2006). The UHP terrane has been proposed to form through intracontinental subduction at the end of collision (Gilotti & McClelland, 2007; Gilotti & McClelland, 2011), and exhumed through vertical extrusion and lateral escape (Gilotti & McClelland, 2007; Hallett et al., 2014).

Migmatitic gneiss with leucosome suggests that the UHP terrane was partially melted. Rare metapelite was partially melted via phengite breakdown on the exhumation path at HP conditions, indicated by phase equilibria (Lang & Gilotti, 2007, 2015). The metapelite displays extensive evidence of partial melting, such as leucosomes with kyanite and garnet, polymineralic inclusions (consisting of kyanite, rutile, K-feldspar, biotite and plagioclase), polycrystalline quartz in restitic garnet, equigranular quartz and euhedral garnet and kyanite crystals (Lang & Gilotti, 2007). The partial melting reaction is inferred to be clinopyroxene+phengite+quartz → garnet+kyanite+K-feldspar+melt (Lang & Gilotti, 2015). Phase equilibrium modelling predicts that the melt composition is granitic, with a modal percentage up to 13 vol%, and that the generated melt crystallized at ~ 1.2 GPa, 825 °C. On the mesoscale, pegmatites and granitoids cross-cutting eclogite pods are deduced to be generated through partial melting of eclogite or quartzofeldspathic gneiss at an early exhumation stage and by fluid-assisted melting at a later stage (Gilotti & McClelland, 2007; Gilotti et al., 2014; McClelland et al., 2009). Zircon from boudin-neck granitoid and cross-cutting pegmatite in eclogite pods yields a range of ages for melting, which started from 347 Ma and continued to 320 Ma (Figure 1c; Gilotti et al., 2014).

3 | OUTCROP AND PETROGRAPHIC DESCRIPTION

Mafic UHP rocks are distributed as lenses and blocks within quartzofeldspathic gneiss on Rabbit Ears Island (Figure 1b). The size of the eclogitic pods varies from metres to tens of metres long (Figure 1c). These pods show compositional variation among bimineralic eclogite, quartz eclogite, kyanite eclogite and garnet-rich layers (Figure 2). The compositional layers are centimetres to decimetres thick and may be isoclinally folded (Figure 2a). Deformed to undeformed pegmatite and granite, commonly 1–10 m thick, occur in outcrop (Figures 1c and 2a,b). The leucosomes are mainly composed of quartz and feldspar, with varying amounts of garnet, amphibole, biotite, epidote and accessory minerals (Gilotti et al., 2014). Pegmatites may contain coarse to very-coarse graphic intergrowths of quartz and feldspar (Gilotti et al., 2014).

Representative kyanite eclogite 03-110 was selected to delineate *P–T* conditions and the melting history of the UHP terrane. The sample was collected from a 40 m wide by 140 m long boudin (Figure 1b,c). Pegmatite within eclogite boudins commonly crosscuts the compositional layers (Figure 2b). Leucosomes may contain dendritic branches parallel to layering that join the crosscutting dykes. Pegmatite located within the large eclogite boudin crosscuts mafic banding (Figure 2b) and displays modal variation of felsic and mafic minerals. The northernmost pegmatite in the large eclogite pod (Figure 1c) contains a melanocratic layer rich in biotite, with graphic intergrowths of quartz and feldspar in the leucocratic part. The pegmatite, where sample 03-111 (Gilotti & McClelland, 2007) was collected (Figure 1c), is characterized by large quartz bands with plagioclase rims showing cusps into the quartz, and displays quartz and K-feldspar intergrowths on the hand-specimen scale, which indicate that the pegmatite crystallized from melt, migrated from partially

This article is protected by copyright. All rights reserved.

melted eclogite. U–Pb ion probe dating of the core and outer mantle of zircon from the pegmatite yielded ages of 353 and 327 Ma, respectively (Gilotti & McClelland, 2007).

Sample 03-110, a medium-grained kyanite eclogite, is from the same location as the previously studied sample 434446 (Gilotti & Ravna, 2002). Textural relationships suggest a peak mineral assemblage of garnet (Grt I), omphacite (Cpx I), kyanite (Ky I), coesite, rutile, clinozoisite and accessory zircon (Figures 3 and 4; Table 1). Garnet I porphyroblasts are anhedral, with grain sizes up to 4 mm in diameter. They comprise ~. 25 vol% of the sample and contain single-phase inclusions of omphacite, kyanite, quartz and rutile, and polymineralic inclusions. Matrix omphacite (Cpx I) is anhedral and replaced by diopsidic clinopyroxene (Cpx II) + plagioclase symplectite. Kyanite (Ky I) forms anhedral porphyroblasts up to 5 mm long, and typically contains quartz and omphacite inclusions. Relic clinozoisite–epidote (Figure 3a), anhedral in shape, is interpreted as part of the peak assemblage.

Petrographic textures indicate that an assemblage of biotite, plagioclase, albite, K-feldspar, amphibole, quartz, with a second generation of garnet (Grt II), clinopyroxene (Cpx II), and kyanite (Ky II), was developed during retrograde stage (Figure 3a–f). Small biotite and plagioclase intergrowths, interpreted as pseudomorphs after phengite, occur locally (Figures 3b and 4a). In the matrix, plagioclase embays omphacite (Figure 3b,c), coexists with amphibole in graphic texture (Figure 3d), is poikiloblastic (Figure 3f), and sends cusps into surrounding phases (Figure 3e,f). Plagioclase in a graphic intergrowth with amphibole shows simultaneous extinction (Figure 3d). Quartz, Ky I and Ky II are commonly rimmed by plagioclase (Figures 3c, e and 4 b–d). The second generation of garnet, showing straight boundaries against plagioclase, grew on partly resorbed Grt I and nucleated in the matrix (Figure 3e,f). Cuspate plagioclase shows low dihedral angles (20–40˚) in boundaries such as those of plagioclase–garnet–omphacite and plagioclase–garnet–garnet (Figure 3d–f). Plagioclase may form strings of beads or poikiloblasts (Figure 3f). Ky II also occurs as clusters in the matrix, enclosed by plagioclase. Cpx II is observed as lamellae, with plagioclase and amphibole, in symplectitic intergrowth replacing omphacite and displaying a decrease of lamellae size from core to rim. Retrograde amphibole and plagioclase replace the peak clinozoisite–epidote (Figure 3a).

The studied sample is characterized by abundant polymineralic inclusions within Grt I and Ky I (Figure 4), where the hosts display radial fractures. These inclusions, which should not be confused with crystallized melt inclusions (Cesare, Ferrero, Salviolo-Mariani, Pedron, & Cavallo, 2009) or multiphase solid inclusions without melt involved (Frezzotti & Ferrando, 2015), are very large (up to 1 mm in diameter). They consist of an aggregate of minerals, with magmatic textures, and of metamorphic relics. Abundant polymineralic inclusions of quartz+ Cpx II±Ky II±plagioclase, without K-feldspar and/or other K-rich phases, are present within Grt I and Ky I (Figure 4b–d). In these inclusions, relicts of partly resorbed metamorphic quartz are located in the cores, while cuspate crystals of omphacite (Cpx II) and plagioclase (Figure 4b–d), with or without enclosed Ky II (Figure 4d), are present between quartz and host. Much more rare polymineralic inclusions of albite+K-feldspar also occur in Grt I (Figure 4a).

The polymineralic inclusions are interpreted as crystallized former large pockets of melt (hereafter called melt pockets), which contain former melt and solid resultant (e.g. peritectic garnet), interacting with the eclogite. Similarly, the cuspate textures observed in matrix and in polymineralic inclusions are considered to represent the original interstitial geometry filled by melt. Other microstructures, such as graphic intergrowths present in the rock matrix suggest that amphibole + plagioclase was crystallized from former melt pockets.

This article is protected by copyright. All rights reserved.

4 | MINERAL CHEMISTRY

4.1 | Analytical methods

The chemical composition of selected minerals was determined using a Cameca SX100 electron microprobe (EMP) equipped with five wavelength dispersive spectrometers at the Institut für Mineralogie und Kristallchemie at Universität Stuttgart, Germany. Natural albite, orthoclase, diopside and rhodonite, and synthetic hematite, periclase, $BaSO_4$, TiO_2, Cr_2O_3 and Al_2O_3 were used for standards. X-ray maps of garnet were obtained using 15 kV accelerating voltage, 70 nA beam current and 60 ms pixel time with step sizes from 5 to 20 μm depending on the size of garnet. Analytical conditions for point analysis were set at 15 kV and 15 nA for garnet and kyanite, whereas 15 kV and 10 nA were used for all other minerals except rutile. The counting time per element was 20 s both on the peak and the background. Rutile was analyzed with 15 kV accelerating voltage, 90 nA beam current and 300 s counting time on both peak and background of the Zr Lα radiation line. The counting time for analyzing Cr, Fe, Nb and Si in rutile was 100 s for both background and peak. Si was measured in order to monitor the possible influence from surrounding silicates. The J43_Zir, wollastonite, Cr_2O_3, Fe_2O_3 and Nb standards were used for analyzing rutile. A beam diameter of 1 μm was used for most analysis. The on-line PAP routine by Cameca was employed for correcting raw counts. Chemical composition was processed and structural formulae were calculated using Excel spreadsheet CALCMIN (Brandelik, 2009) for all analyzed minerals except amphibole. The amphibole analyses were processed with the Excel spreadsheet by Locock (2014) and classified according to the nomenclature of Hawthorne et al. (2012). Representative analyses of minerals in samples 03-110 are listed in Table 2.

4.2 | Analytical results

Garnet porphyroblasts in kyanite eclogite 03-110 exhibit compositionally homogeneous cores and slightly zoned rims (Figure 5a–d) with the spessartine (Sp) content < 0.02. The composition of Grt I cores is $Gr_{36}Alm_{28}Py_{35}$, with Gr, Alm and Py referring to grossular, almandine and pyrope respectively (Figure 5). The grossular content of the garnet rim is lower (Gr_{27}) than in the core. Almandine shows a gradual increase from Alm_{27} to Alm_{36} at the outermost rim. Pyrope increases slightly from Py_{34} to Py_{36} and decreases to Py_{35} at the outermost rim (Figure 5a). Omphacite (Cpx I) is zoned, with a high jadeite (Jd) core, X_{Jd} = 0.38, and a low jadeite rim, X_{Jd} = 0.18. Normalized chemical composition of omphacite contains Fe^{3+} up to 0.06 p.f.u. (per formula unit), using a charge balance method for normalization. Kyanite (Ky I) has a composition of nearly pure aluminosilicate with a small amount of Fe, assumed to be Fe^{3+}, up to 0.01 p.f.u.

The retrograde Grt II is richer in pyrope and almandine and poorer in grossular ($Py_{40}Alm_{37}Gr_{23}$) than Grt I (Figure 6). Compared with the core of matrix omphacite, Cpx II surrounding quartz in garnet is lower in jadeite (X_{Jd} up to 0.35). Cpx II in the melt domain (Figure 5e–h) is omphacite to diopside, with X_{Jd} varying from 0.11 to 0.29. Cpx II in symplectite is diopside, with a wide range of composition. Thicker lamellae commonly have a higher jadeite content, with X_{Jd} = 0.15–0.21, whereas in the thinner lamellae X_{Jd} ranges from 0.05–0.15. Ky II, smaller in size and occurring as clusters, is similar to Ky I in composition. Amphibole composition varies in different domains. The amphibole in the matrix and crystallized melt is pargasite with 0.45–0.60 p.f.u. for Na in the A-site and 6.2–6.5 Si p.f.u. Calculated Fe^{3+} content in amphibole is up to 0.45 p.f.u.; in the graphic intergrowth with plagioclase, the calculated Fe^{3+} content is only 0.15 p.f.u. Amphibole in symplectite after omphacite is calcic, either pargasite or magnesio-hornblende, with 0.23–0.47 p.f.u Na in A-site, and 6.58–7.06 Si p.f.u. with up to 0.20 p.f.u. Fe^{3+}. Plagioclase enclosed in garnet, in the matrix, in intergrowths with biotite and amphibole, and in symplectite with Cpx II contains a small amount of K-feldspar component, with X_{Kfs} value (=K/(Na + Ca + K)) about

This article is protected by copyright. All rights reserved.

0.02, and varies from oligoclase to andesine, with X_{Ab} value (=Na/(Na + Ca + K)) ranging from 0.64–0.77. Plagioclase in the crystallized melt domain (Figure 6) is oligoclase (X_{Ab} = 0.72–0.76) with X_{Kfs} = 0.01. Plagioclase in symplectite with clinopyroxene (Cpx II) and amphibole has an oligoclase core (X_{Ab} = 0.70–0.74) and an andesine rim (X_{Ab} = 0.59–0.67). Rare K-feldspar in crystallized melt pockets in garnet and kyanite is a nearly pure phase (X_{Kfs} > 0.98). Biotite is characterized by a Ti content ranging from 0.10–0.13 p.f.u. and X_{Mg} (=Mg/(Mg+Fe)) from 0.79–0.82.

Rutile appears as inclusions in garnet and as a matrix mineral; exsolved ilmenite is observed in some rutile grains. Detailed line scans of large rutile (100 μm) reveal no systematic zoning. Rutile in garnet contains 620–890 ppm Zr, whereas Zr in matrix rutile ranges from 570–760 ppm.

5 | PHASE EQUILIBRIUM MODELLING

5.1 | Modelling techniques

An isochemical phase equilibrium diagram, which is also known as a pseudosection (Powell, Holland, & Worley, 1998), was constructed to estimate *P–T* conditions for the eclogite, assuming equilibrium at whole rock or domainal scale. Phase diagrams for particular bulk rock and domainal compositions were modelled based on the principle of Gibbs Free Energy minimization, using the software package PERPLE_X (version 6.7.7 from March 2017; Connolly, 2005) along with the internally consistent thermodynamic dataset of Holland and Powell (2011) for minerals and H_2O (with the CORK equation).

A phase diagram for the bulk rock was constructed within the 11-component system MnNCKFMASHTO (MnO-Na_2O-CaO-K_2O-FeO-MgO-Al_2O_3-SiO_2-H_2O-TiO_2-O_2). This system was chosen for its capacity to model geologically realistic phase diagrams (Massonne, 2014, 2015). An amount of oxygen, equivalent to some Fe^{3+} in the rock, and a free fluid phase of pure H_2O were considered. Prograde metamorphism may release oxygen and H_2O, which may influence the stability of mineral assemblages. For example, breakdown of lawsonite and chlorite can release water and oxygen (e.g. Ferrando, Frezzotti, Petrelli, & Compagnoni, 2009; Groppo & Castelli, 2010), which tend to leave the system. The incorporation of Fe^{3+} will influence the *P–T* field of minerals such as clinopyroxene, amphibole and epidote (Diener & Powell, 2010; Petrie, Massonne, Gilotti, McClelland, & Van Staal, 2016; White, Powell, Holland, & Worley, 2000), thus a reasonable estimation of the true Fe^{3+} content in the bulk-rock is important. A small amount of K is mainly hosted by mica, and to a lesser extent by amphibole and feldspar; therefore, K_2O is retained in the calculations. Titanium is mainly hosted in rutile and biotite, which are important minor phases in the studied rocks.

A *P–T* phase diagram for a partially melted domain (Figure 6) was calculated in the 9-component system MnNCFMASHO to understand conditions of melting and melt crystallization. Manganese is included in the system to monitor garnet-in boundaries. Minor elements, K and Ti, have been analyzed in minerals in the partially melted domain (e.g. K in plagioclase and amphibole, Ti in amphibole and garnet) (Table 2); however, these elements with low concentration in the domains were eliminated from the calculation because the activity-composition models utilized cannot accommodate them (e.g. Ti in garnet). An isochemical phase equilibrium diagram for the symplectite after omphacite was constructed in the 8-component NCKFMASH system to further constrain the conditions of its formation. Titanium, Mn and Fe^{3+} were excluded from the system because of their low abundance in omphacite.

This article is protected by copyright. All rights reserved.

Solid-solution models for clinopyroxene (including diopsidic clinopyroxene and omphacite) (Diener & Powell, 2012; Green, Holland, & Powell, 2007), amphibole (Green et al., 2016), garnet, white mica, biotite (White, Powell, Holland, Johnson, & Green, 2014), and feldspar (Fuhrman & Lindsley, 1988) are used. Garnet in the sample contains only small amounts of spessartine, thus this endmember was restricted to 10 mol% in the garnet solution model. Lawsonite, kyanite, coesite, quartz and rutile are treated as pure phases. Zoisite in the diagram for the symplectite after omphacite is also treated as a pure phase. Talc (Holland & Powell, 2011), chlorite, ilmenite (White et al., 2014), and spinel (White, Powell, & Clarke, 2002) were considered but not observed in the models.

As natural zoisite may incorporate some Fe^{3+} that may stabilize it to a higher pressure and temperature (Gottschalk, 2004; Mattinson, Zhang, Tsujimori, & Liou, 2004; Poli & Schmidt, 2004), we tried to consider this by creating a solid-solution model for Fe^{3+}-bearing zoisite. The clinozoisite end-member (cz) was replaced by the zoisite end-member (zo) in the epidote solution model of Holland and Powell (2011). Therefore, the epidote model refers to the epidote-group minerals, including zoisite, epidote and Fe-epidote.

A solution model for modelling melting of metabasite at pressures higher than 1.3 GPa does not exist yet (Green et al., 2016; Palin, White, & Green, 2016). Phase equilibrium modelling was conducted using the recently published tonalitic to trondhjemitic melt solution model (Green et al., 2016), aimed at modelling melting of the eclogite. Extrapolation of the melt model to eclogite may yield uncertainties because it was originally calibrated for melting at < 1.3 GPa; however, the solution model has been extended to melting of metabasite at pressures up to 2.6 GPa (Wade, Dyck, Palin, Moore, & Smye, 2017), and has produced geologically realistic results. To minimize the number of pseudocompounds during calculation, the keyword values for initial_resolution and final_resolution in the perplex_option.dat file were modified from 0.067 to 0.100 and from 2.5e-4 to 5e-3, respectively. Iteration value 2 and refinement_points_II were decreased to 1. The compositional range of the amphibole and melt models in file solution_model.dat of PERPLE_X was limited iteratively.

An effective bulk composition is critical for applying phase equilibrium modelling to natural mineral assemblages (Lanari & Engi, 2017 and references therein). *P–X* diagrams are used for understanding the influence of composition (*X*) on the topology of the phase diagrams. *P–X*(H_2O) (Figure 7) and *P–X*(CaO) (Figure 8) diagrams are presented to illustrate influences of these two components and *P–X*(H_2O) diagram also used to determine the amount of H_2O for modelling *P–T* diagram. *P–T* diagrams (Figures 9–11) are used to estimate metamorphic conditions, along with detected mineral compositions and mineral isopleths.

5.2 | Effective Bulk Composition

The whole-rock bulk composition was obtained using a wavelength dispersive X-ray fluorescence (XRF) spectrometer at Washington State University. The sample composition (Table 3) was modified for the 11-component system. The CaO was reduced by the amount of P_2O_5 assuming that all P_2O_5 was bound to pure apatite (Massonne, 2014). *P–X*(O_2) diagrams were modelled to determine the influence of oxygen on the boundaries of specific assemblage fields. For the O_2 range corresponding to 0–20 % Fe^{3+}, little influence on the phase boundaries was noted. A small amount of Fe^{3+} exists in omphacite and amphibole, thus oxygen was estimated to correspond to Fe^{3+} = 5% of the total iron. Crystallization of

This article is protected by copyright. All rights reserved.

Accepted Article

porphyroblasts fractionates elements from the bulk rock (e.g. Marmo, Clarke, & Powell, 2002; Stüwe, 1997; Tinkham, Zuluaga, & Stowell, 2001; Zuluaga, Stowell, & Tinkham, 2005), although the high temperature experienced by the kyanite-eclogite probably induced strong diffusion.

The crystallized melt pocket (Figure 6) and a symplectite after omphacite were selected for detailed petrological study. These micro-domains render the XRF-derived bulk composition inaccurate for modelling retrograde conditions. Partial melting and symplectite formation may occur in an open system (e.g. Martin & Duchene, 2015; Massonne, 2012; Palin, St-Onge, Waters, Searle, & Dyck, 2014; Weinberg & Hasalova, 2015) or a closed system (Bigge, Martin, & Harlow, 2016); therefore, care needs to be taken when applying isochemical phase equilibrium diagrams to a fixed bulk composition of a microdomain. Nonetheless, such an approach has been used to generate meaningful *P–T* conditions for a symplectite after omphacite in a partially open system (Tedeschi et al., 2017), and is employed to model two microdomains in this study. A crystallized melt pocket was selected for examining the melting and recrystallization conditions (Figure 10A). The effective bulk composition was obtained by incorporating the proportion and composition of minerals that appear to be equilibrated with each other. Equilibrium proportions of the amphibole, clinopyroxene, plagioclase and garnet are estimated to be 14.8, 25.5, 39.2 and 20.3 vol%, respectively. Phase densities chosen from minerals with similar composition are 3.21 g/cm^3 for amphibole (Oberti, Ungaretti, Cannillo, Hawthorne, & Memmi, 1995), 3.29 g/cm^3 for clinopyroxene (Mottana, Rossi, Kracher, & Kurat, 1979), 2.64 g/cm^3 for plagioclase (Phillipsi, Colville, & Ribbe, 1971) and 3.7 g/cm^3 for garnet (Nestola et al., 2012). Local bulk composition of the examined symplectite after omphacite was obtained using EMP analyses on thin mineral lamellae with an enlarged beam size (20 μm). A total of 15 spots were analyzed and averaged to provide an effective bulk composition (Table 3). Water content for both the melt pocket and the symplectite was estimated from hydrous minerals in these domains.

5.3 | Petrological Modelling Results

5.3.1 | *P–X*(H_2O) diagram

Water plays a crucial role in metamorphism, inducing partial melting and developing retrograde textures (e.g. Guiraud, Powell, & Rebay, 2001; Martin & Duchene, 2015; Spruzeniece, Piazolo, Daczko, Kilburn, & Putnis, 2016; Weinberg & Hasalova, 2015); therefore, the amount of water is critical to determining the position of solidus curves and mineral phase relations (e.g. Lang & Gilotti, 2015). A *P–X*(H_2O) diagram was calculated at 900 °C for the studied sample, with H_2O content varying from 0–1 wt% (Figure 7), normalized to a total of 100% for both ends of the horizontal axis. Phase relations of melt with respect to trace amounts of water and phengite do not show a large change at > 2.8 GPa. The H_2O saturation curve (H_2O-in curve) is located from 2.7 GPa at 1.00 wt% H_2O to 2.8 GPa at 0.05 wt% H_2O (Figure 7a). A lower water content results in coexistence of phengite and sanidine, which has not been observed. The phengite-out curve is located at 2.2 GPa with H_2O content ranging from 0 to ~ 0.15 wt%; this curve extends up to 2.8 GPa increasing H_2O to 0.30 wt%, and remains constant at 2.8 GPa with increasing H_2O to 1.0 wt%. The amphibole-in-curve is predicted at 1.8 GPa. With increasing water content, melt modes increase from 0 without water, to up to 15 vol% at 1 wt% H_2O and amphibole modes increase to 32 vol% in melt-absent fields (Figure 7b). Since a small amount of crystallized melt (< 5 vol%) is observed in the studied sample, an arbitrary value of 0.3 wt% of water is selected for further modelling. With this amount of water at 900 °C, melt is predicted to be present at pressures from 1.6 to 2.8 GPa.

This article is protected by copyright. All rights reserved.

5.3.2 | *P–X*(CaO) diagram

A *P–X*(CaO) diagram, modelled at 900 °C, was used to evaluate the effect of the bulk CaO content on the phase boundaries. With CaO varying from 10–15 wt% and totals of both ends of the horizontal axis normalized to 100%, the constructed *P–X*(CaO) diagram for sample 03-110 (Figure 8) shows that Ca strongly affects the phase boundaries and mineral compositions. The upper limit of epidote-group minerals is strongly influenced by the CaO content (Figure 8a), where higher CaO extends the upper limit toward a higher pressure.. At 900 °C, an epidote-group mineral is present at UHP conditions with 12.5 wt% CaO and the upper limit can reach 3.8 GPa at 15 wt% CaO. The XRF-derived bulk CaO content of the sample is 11.3 wt%, which agrees with the absence of epidote-group mineral at 900 °C. Grossular-in-garnet (X_{Gr}) increases with increasing *X*(CaO) in the epidote- and feldspar-absent fields; in the feldspar-present fields, it is mostly pressure dependent (Figure 8b). The upper limit of the melt-in curve is rather constant at 2.8 GPa, whereas the lower limit decreases from 1.65 to 1.3 GPa and then increases to 1.5 GPa with increasing CaO.

5.3.3 | *P–T* phase diagrams

The *P–T* diagrams for sample 03-110 (Fig. 9a) were constructed with an adjusted bulk rock composition (see Table 3). Mineral compositions are given by isopleths, including X_{Gr}-, X_{Py}- and X_{Alm}-in-garnet, X_{Jd}-in-clinopyroxene, and modal epidote-group mineral, melt and garnet (Figure 9b,c). Garnet, clinopyroxene and rutile are everywhere present (Figure 9a). With the low water content, a small amount of free fluid is present at > 2.1 GPa. The melt-in curve at > 2.1 GPa has a positive *dP/dT* slope. The position of the solidus curve is closely associated with the location of the hydrous phases (e.g. epidote-group minerals and phengite). Epidote-group minerals are present at UHP from 660 to 670 °C, and the upper limit decreases to lower pressure with increasing temperature. The upper temperature limit of the epidote-group mineral is ~ 890 °C at 1.9 GPa. Amphibole is present at lower pressure and lower temperature with the amphibole-out curve having a negative slope; the upper-pressure limit of amphibole reaches ~ 2.4 GPa at 650 °C and decreases to 1.1 GPa at 1000 °C.

The deduced peak mineral assemblage – phengite, garnet, omphacite, kyanite, coesite, epidote-group mineral and rutile – is located in the *P–T* region at 2.9 GPa, 660–670 ˚C. This field shows a garnet composition of X_{Gr} = 0.33, X_{Alm} = 0.32, X_{Py} = 0.34 and an omphacite composition of X_{Jd} = 0.14. The analyzed garnet does not match the modelled composition in the epidote-present field. The garnet core (X_{Gr} = 0.36, X_{Alm} = 0.28, X_{Py} = 0.35) plots at 3.4 GPa, 940 ˚C with the coexisting mineral assemblage of phengite, garnet, omphacite, kyanite, coesite, rutile and a small amount of water in the phase diagram. Omphacite at this *P–T* condition has X_{Jd} = 0.37, which is close to the highest X_{Jd} value of analyzed omphacite (X_{Jd} = 0.38). The mineral assemblage, without epidote, occupies the largest *P–T* area on the modelled phase diagrams at UHP. The garnet mode at 3.4 GPa and 940 ˚C is about 32 vol%, which is higher than the observed mode of 22%. Garnet is anhedral due to retrograde resorption, indicating that the volume percentage at peak conditions was higher than the observed mode. The peak *P–T* condition given by garnet isopleths, rather than the epidote-bearing mineral assemblage, is taken as the best estimate.

Phase equilibrium modelling of a crystallized melt pocket (Figure 6) was conducted to understand the melting and crystallization conditions (Figure 10; Table 3). Garnet and clinopyroxene are ubiquitous within the modelled *P–T* range. The modelled phase diagram displays a solidus curve with a positive *dP/dT*-slope at > 2.0 GPa, and a negative slope below this pressure (Figure 10a). With a higher amount of water, the solidus migrates toward lower temperature conditions. The observed mineral assemblage of amphibole, feldspar, garnet and clinopyroxene occupies a large area at 1.0–1.4 GPa across the calculated temperature range. Compositional isopleths for garnet, clinopyroxene and plagioclase are plotted (Figure 10b,c);

This article is protected by copyright. All rights reserved.

the rim of Grt II (X_{Alm} = 0.38, X_{Py} = 0.38, X_{Gr} = 0.23) yielded suprasolidus conditions of 1.4 GPa, 900 ˚C. These estimates are right above the modelled solidus curve and close to the solidus of experimental (Q. Liu et al., 2009; Skjerlie & Patiño Douce, 2002) and theoretical (Vielzeuf & Schmidt, 2001) studies. The core of omphacite (Cpx II; X_{Jd} = 0.29) suggests a pressure of 1.9 GPa, while the clinopyroxene rim with lower X_{Jd} indicates equilibration at a lower pressure. The composition of plagioclase (X_{Ab} = 0.72) and clinopyroxene (X_{Jd} = 0.15) intersect at about 1.3 GPa, 720 ˚C, which is interpreted as the equilibrium *P–T* of the crystallized assemblage.

The phase diagram in Figure 11 shows a *P–T* range for the formation of the symplectite after omphacite. Due to using the NCKFMASH system, phengite occurs at higher pressure with the phengite-out curve displaying a positive *dP/dT* slope from 1.1 GPa, 650 ˚C to 2.0 GPa, 900 ˚C. The assemblage of amphibole+clinopyroxene+feldspar with a trivial amount of free fluid covers a large area at 1.0–1.7 GPa, 680–1000 ˚C. In this field, X_{Jd} in clinopyroxene varies from 11 to 16 mol%, which agrees with the measured clinopyroxene composition (Figure 11b). Only a minor amount of K is considered for the modelling, thus feldspar is essentially plagioclase. The feldspar in the *P–T* field of clinopyroxene+amphibole+plagioclase contains 61 to 66 mol% albite, in agreement with the analyzed plagioclase (Figure 11b). The symplectite probably evolved over the large *P–T* field on the exhumation path, and is thus not used to determine an exact equilibration condition.

6 | EMPIRICAL AND TRACE ELEMENT THERMOBAROMETRY

6.1 | Amphibole–plagioclase thermometry

Amphibole–plagioclase thermometry (Holland & Blundy, 1994) was used to evaluate the *P–T* conditions for crystallization of the melt domain (Figure 5e–h). Since quartz is absent in this crystallized melt pocket, only the edenite–richterite thermometer based on the reaction of edenite + albite = richterite+anorthite could be used. The thermometer gives an uncertainty of ± 40 °C. A temperature of 717 °C was obtained using the representative composition of amphibole and plagioclase from the crystallized melt pocket (Table 2) at an estimated 1.3 GPa, which was derived from isopleths of clinopyroxene, amphibole and plagioclase in the modelled phase diagram. Using the same thermometry, the composition of amphibole and plagioclase (Table 2) in the symplectite yielded an equilibrium temperature of 732 °C at 1.3 GPa.

6.2 | Zr-in-rutile thermometry

Rutile incorporates Zr in its crystal structure and is saturated with this element when in equilibrium with SiO_2 and zircon. The amount of Zr in rutile is mainly temperature dependent, and has been utilized as a single-mineral thermometer (Zack, Moraes, & Kronz, 2004). Since the studied sample contains quartz and zircon, this thermometer can be applied. Experiments have demonstrated that pressure influences the Zr-in-rutile thermometer (Tomkins, Powell, & Ellis, 2007; Watson, Wark, & Thomas, 2006). For this reason, the calibration after Tomkins et al. (2007) was used, which contains an uncertainty of ± 30 °C (2 σ). Rutile enclosed in garnet yields 781–817 °C at 3.4 GPa, and 726–758 °C at 1.8 GPa. Matrix rutile gave 773–801 °C at 3.4 GPa At 1.8 GPa, the temperature range for the matrix rutile (718–744 °C) is lower.

7 | DISCUSSION

The *P–T* path for the kyanite eclogite (Figure 12) displays a slightly different position and shape than the one deduced by Lang and Gilotti (2015) for metapelites from the UHP terrane. This might be caused by uncertainties in mineral analyses and the applied thermodynamic database and solution models (e.g. Palin, Weller, Waters, & Dyck, 2016). Our path has an

This article is protected by copyright. All rights reserved.

Accepted Article

inferred prograde path and an exhumation path containing a decompression segment with slight cooling followed by a strong cooling segment (Figure 12).

7.1 | Prograde and peak pressure stages

Delineating the prograde *P–T* evolution of the UHP kyanite eclogite is challenging due to a HP history of over 50 million years of crustal thickening caused by the Caledonian collision before a late stage of UHP via intracontinental subduction (Gilotti & McClelland, 2007). Figure 12 shows a dotted line originating at approximately 1.8 GPa and 800 °C that represents the path from the HP metamorphism at 425–390 Ma to our peak UHP estimate at 365–350 Ma. Temperature estimates of ~750 °C for matrix rutile and ~760 °C for rutile inclusions at 1.8 GPa in garnet corroborate the prograde path. A tectonic setting at the base of an overthickened crustal welt is consistent with this prograde path and the high peak UHP temperature estimate. Subsequent diffusion also modified the peak-*T* estimate. Fast diffusion at high temperature, coupled with a long resident time at UHP, has erased any prograde garnet zoning. At a high temperature (~ 900 ˚C) and a long residence time (10 Ma), diffusion will fully homogenize centimetre-sized garnet (Caddick, Konopásek, & Thompson, 2010). Grt I, which is smaller than 1 cm and displays a homogeneous core (Figures 5 and 6), has been homogenized due to a residence time of at least 15 Ma at UHP (Gilotti et al., 2014; McClelland et al., 2006). The presence of single phase inclusions such as omphacite and kyanite in garnet cores indicates entrapment during the eclogitization and subsequent prograde to peak metamorphic stage. Zr-in-rutile thermometry for matrix grains and inclusions in garnet yielded ~800–820 ˚C at 3.4 GPa, indicating that they were already formed on the prograde path.

Peak pressure was attained under subsolidus conditions within the coesite stability field (Figures 9b and 12). The estimated *P–T* (3.4 GPa, 940 ˚C) from isopleths of garnet (Grt I) is taken as the calculated peak condition. This *P–T* condition is lower than the previous estimate of 3.6 GPa, 972 ˚C (Gilotti & Ravna, 2002) calculated using garnet-clinopyroxene-kyanite-phengite-coesite empirical thermobarometry (Ravna & Terry, 2004). The deviation is attributed to the uncertainties in both methods. The garnet-clinopyroxene-phengite thermobarometry has an error range of ± 0.32 GPa and ± 65 °C in the coesite field (Ravna & Terry, 2004). Massonne (2013) suggested errors of 10% for pressure, and 5% for temperature from phase equilibrium modelling, which would lead to an error of ± 0.3 GPa and ± 45 °C.

7.2 | Retrograde development of the UHP kyanite eclogite

7.2.1 | Initial Exhumation

The *P–T* path for initial exhumation of the UHP eclogite is difficult to determine. An exhumation path with strong cooling forms hydrous minerals (e.g. epidote-group mineral at 2.3 GPa, 750 °C and amphibole at 2.1 GPa, 750 °C), as predicted by the modelled diagram with a relatively limited water content (Figure 9a). Due to the dry nature of eclogite at UHP (e.g. Zheng et al., 2011), formation of hydrous minerals typically requires external fluid (Massonne, 2012; Palin et al., 2014). However, such flux of fluid into the system at > 800 °C would lead to fluxed melting of the eclogite (Weinberg & Hasalova, 2015). The garnet compositional contours from core to rim point to an exhumation path with strong cooling, along which the garnet mode decreases; this contradicts the observed increase of garnet modes, and thus renders the modelled phase diagram unsuitable for deciphering retrograde conditions. As discussed below, a *P–T* path with slight cooling is more likely for exhumation.

This article is protected by copyright. All rights reserved.

7.2.2 | Evidence for partial melting of the eclogite

Crystallized melt pockets are common in the studied UHP eclogite, both in the matrix and as inclusions in garnet (Figures 3b,c,e,f and 4b–d). The cuspate boundaries are interpreted as melt-solid boundaries, where the cuspate grain (e.g. plagioclase) was crystallized from melt and surrounding minerals (e.g. garnet) were solid (e.g. Brown, 2001; Harte, Hunter, & Kinny, 1993; Holness & Sawyer, 2008; Rosenberg & Riller, 2000). Dihedral angles at plagioclase–solid–solid boundaries in the studied samples fall in the range of measured melt–solid–solid dihedral angles for plagioclase (e.g. Holness, 2006; Jurewicz & Watson, 1984; Laporte, Rapaille, & Provost, 1997; Longhi & Jurewicz, 1995), corroborating the interpretation of such textures as due to former melt.

Graphic intergrowths are present in kyanite eclogite 03-110 and pegmatite 03-111 (Figure 1c). Such textures have been documented in numerous rock types with different mineral assemblages; for example, pyroxene and plagioclase in basalt (Beaty, Hill, Albee, & Baldridge, 1979) and dolerite (Vernon, 2004), plagioclase and K-feldspar in gneiss (Braun, Raith, & Kumar, 1996), diopside and feldspar, and albite and K-feldspar in leucocratic veins (Bakker & Elburg, 2006), and albite, amphibole and clinopyroxene in pegmatite (Nijland & Touret, 2001). The formation of graphic textures has been attributed to hydrothermal replacement (e.g. Bakker & Elburg, 2006; Nijland & Touret, 2001) or melt crystallization (e.g. Fenn, 1986; Lentz & Fowler, 1992; London & Morgan, 2012). Hydrothermal replacement is unlikely to be the mechanism for the graphic intergrowth of amphibole and plagioclase, because the existence of water would have triggered extensive melting of the eclogite at high temperature, which is not the case for the studied eclogite. The graphic intergrowth of amphibole and plagioclase is interpreted to have formed by crystallization of a pre-existing hydrous melt. Large pargasite (Figure 3d) crystallized from the melt pocket first enriching the remaining melt in silica. With further cooling, pargasitic amphibole, plagioclase and quartz crystallized. The graphic texture formed because undercooling may have inhibited nucleation of new minerals, favoring epitaxial growth along crystalline structures of already formed grains of amphibole and plagioclase (e.g. Fenn, 1986; London & Morgan, 2012; Smith, 2012).

Polymineralic inclusions within garnet and kyanite show cusps and embayments indicating that the UHP eclogite was partially melted (Figure 4). The inclusions contain relict metamorphic phases and minerals crystallized from melt, suggesting that former melt pockets interacted with surrounding minerals or rocks (e.g. Ferrero et al., 2012). Large polymineralic inclusions were also documented in eclogite and calc-silicate gneiss from the Dabie UHP terrane (Y. X. Chen et al., 2014; Gao et al., 2014; P. L. Liu et al., 2014), which are ascribed to crystallization of partial melt derived from hydrous minerals (e.g. phengite and epidote-group minerals).

On the mesoscale, a pegmatite vein with intermediate composition was formed within the eclogite boudin (Figures 1c and 2b). Since the pegmatite is located in the eclogite pod and cross-cuts the foliation, partial melting of the eclogite pod best explains its origin. This further supports that the studied eclogite pod was partially melted.

7.2.3 | Melting reactions

The documented textures demonstrate that the UHP eclogite was partially melted. Rare K-feldspar-bearing inclusions of melt in garnet (Figure 4a) and biotite+plagioclase cusps into omphacite in the matrix (Figure 3a) indicate that phengite has contributed to initial melting. The polymineralic inclusions of albite+K-feldspar (Figure 4a) were formed through crystallization of granitic (*senso lato*) melt formed from the melting reaction, whereas biotite and plagioclase crystallized from the melt in the matrix. The incongruent melting reaction of

This article is protected by copyright. All rights reserved.

Accepted Article

phengite+ omphacite+quartz → amphibole±garnet+melt (Q. Liu et al., 2013) best explains the melt composition and textures. However, the rare occurrence of these polymineralic inclusions indicates that phengite-driven melting is not significant in the studied eclogites.

In contrast, the more abundant inclusions of clinopyroxene+quartz±kyanite±plagioclase (Figure 4b–d) in garnet and crystallized melt pockets in matrix (Figure 3) are interpreted as products from an intermediate melt. Grt II is more Mg- and Fe-rich, and lower in Ca than Grt I (Figure 6; Table 2). The plagioclase, as oligoclase, contains a non-negligible amount of Ca. Pargasitic amphibole in the crystallized melt pocket contains 0.46–0.59 p.f.u. Na in A-site and 1.79–1.86 p.f.u. Ca in M4 site. Although mineral compositions could have been re-equilibrated during the retrograde stage, their Ca-rich nature suggests a Ca-rich phase as the source. Amphibole melting is unlikely as no amphibole was present at > 2.5 GPa, indicated by phase equilibria (Figures 9 and 10) and observed petrographically. Amphibole melting also requires heating to cross the steep *dP/dT* slope of amphibole-out boundaries on calculated or experimental phase diagrams (e.g. Rapp & Watson, 1995), which is not the case for exhumation of the UHP kyanite eclogite. Incongruent melting of an epidote-group mineral best explains the composition and mineral assemblage in melt pockets. A reaction of epidote-group mineral+ omphacite+quartz → melt+kyanite+diopsidic clinopyroxene±garnet is seen in experimental melting of natural zoisite eclogite at HP conditions (Skjerlie & Patiño Douce, 2002). Quartz, jadeite component in omphacite and an epidote-group mineral partially melted in the experiments using the Verpenesset eclogite (Norway), forming a hydrous melt, Ky II, Cpx II and peritectic garnet (Grt II) (Skjerlie & Patiño Douce, 2002). Rare coarse-grained relicts of clinozoisite partially replaced by amphibole and plagioclase, which shows cusps into adjacent phases in our sample, suggests melting of an epidote-group mineral.

Mineral assemblages in the leucosomes and phase equilibria (Figure 9) reveal that the generated melt is intermediate in composition. The pegmatite vein in the eclogite pod, interpreted as crystallized melt, contains high proportions of quartz and plagioclase, and a relatively small amount of biotite and amphibole, which suggests melting of epidote-group minerals with minor involvement of phengite. The phase diagram predicts that the first droplet of melt is granitic close to solidus at > ~2.0 GPa, and that the melt becomes more trondhjemitic with decreasing pressure and increasing temperature.

7.2.4 | Partial melting conditions

Partial melting of the eclogite occurred on the exhumation path. Due to the limited application of melt solution models at HP and UHP (Green et al., 2016; Holland & Powell, 2001), the phase diagram (Figure 9) for the bulk rock is not exclusively utilized to determine the *P–T* conditions of melting, but experimentally determined phase relations are considered as well. The phase relations from Skjerlie and Patiño Douce (2002) are particularly relevant to our example, because the zoisite-bearing Verpenesset eclogite has a similar bulk composition. Phase relations from experiments on eclogite and theoretical calculation on mafic rocks with respect to wet solidus of basalt are shown in Figure 12 (Kessel, Ulmer, Pettke, Schmidt, & Thompson, 2005; Q. Liu et al., 2009; Vielzeuf & Schmidt, 2001).

At the estimated peak *P–T*, melt was not present in any experiments on mafic composition (Figure 12). Instead, the solidus curve of incongruent melting is initially crossed at HP conditions on the retrograde path with slight cooling (Figure 12). The first melting curve crossed during exhumation of the studied eclogite is the phengite breakdown curve (Q. Liu et al., 2009; Skjerlie & Patiño Douce, 2002). Phengite melting may occur with matrix minerals of omphacite and quartz as reactants, and forms kyanite, plagioclase and melt with or without garnet (Fig. 12; Q. Liu et al., 2009; Q. Liu & Wu, 2013).

This article is protected by copyright. All rights reserved.

Another melting reaction encountered during exhumation is the zoisite breakdown melting (Fig. 12; Skjerlie & Patiño Douce, 2002). During further exhumation of the studied rock to ~2.2 GPa, 920 °C, an epidote-group mineral, omphacite and quartz reacted to form melt, kyanite, garnet and diopsidic clinopyroxene (Skjerlie & Patiño Douce, 2002). Peritectic garnet grew during the partial melting, with the last garnet rim formed under suprasolidus *P–T* conditions at 1.4 GPa, 900˚C (Figure 12; Table 2). The melt pockets may have connected as indicated by the plagioclase poikiloblasts, leading to possible melt loss to form leucocratic veins at the mesoscale. Residual melt pockets crystallized with further decompression and cooling, forming the cuspate boundaries, graphic intergrowth and inclusions of melt within host minerals.

The mineral assemblage of clinopyroxene, amphibole and plagioclase crystallized from generated melt during cooling and exhumation. An exact crystallization condition is unattainable from the modelled phase diagrams, but the empirical amphibole-plagioclase thermometry (Holland & Blundy, 1994) indicates that the assemblage of amphibole+plagioclase+ clinopyroxene equilibrated at 1.3 GPa, 717 ˚C during further cooling. A similar temperature of 725 ˚C is obtained for zircon, interpreted as crystallized from melt, in a granitoid within quartzofeldspathic gneisses from the same outcrop (Gilotti et al., 2014). The cooling rate from peak temperature conditions was probably low, because of the lack of supercooled melt (i.e. glass) in the samples, and the long duration of exhumation recorded by zircon in leucocratic melts (Gilotti et al., 2014). These authors calculated a cooling rate of 11 ˚C/Ma from ~950 ˚C at UHP to 725 ˚C at HP over a ~20 Ma span.

Partial melting may have occurred within garnet or kyanite (Perchuk, Burchard, Maresch, & Schertl, 2008; Perchuk et al., 2009), if clinopyroxene, zoisite and quartz coexisted; but melting in the matrix is more likely due to coexistence of the reacting minerals. Newly formed garnet II grew on preexisting garnet and thus enclosed the melt along with other minerals. Crystallization of the melt took place above the jadeite-albite transformation, leading to the formation of omphacite to diopsidic clinopyroxene (X_{Jd} up to 0.34) and cracks in host minerals due to volume increase (Figure 4). Newly formed garnet or kyanite may not fully enclose the melt pocket. In such cases, crystallization of melt in the matrix is under lithostatic pressure (Figure 10), below the jadeite–albite reaction curve, leading to the crystallization of plagioclase rather than clinopyroxene in the melt domain (Figure 4d).

7.2.5 | Symplectite formation

An isochemical phase equilibrium diagram for a symplectite after omphacite yielded a *P–T* estimate of 1.0–1.7 GPa, 680–1000 ˚C, which is located in the field with an assemblage of clinopyroxene (Cpx II)+amphibole+feldspar and a small amount of free fluid (Figures 11 and 12). The temperature estimate by amphibole-plagioclase thermometry, 730 ˚C at 1.3 GPa falls within the *P–T* range. This *P–T* range is similar to the estimate for the crystallized melt pocket; however, the development of symplectite is a dynamic process. Joanny, Vanroermund, and Lardeaux (1991) demonstrated that symplectite with thinner lamellae towards the unreacted mineral develop at progressively lower temperature. Martin (2018) showed that amphibole in the symplectite postdates the symplectite of clinopyroxene and plagioclase. The symplectitization process, forming Cpx II+amphibole+feldspar after omphacite, requires water or a reactive fluid (Spruzeniece et al., 2016). Such fluid could be derived internally, such as from hydroxyl in omphacite and residual water in grain boundaries (Martin & Duchene, 2015), or externally by diffusion or migration into the system from surrounding domains (e.g. melt pockets) (e.g. Martin, 2018; Massonne, 2012; Palin et al., 2014). Internal fluid, which is limited at UHP, cannot be the single source for sysmplectite with a high amount of amphibole, but can provide fluid for symplectite with little amphibole or without the hydrous mineral.

This article is protected by copyright. All rights reserved.

Accepted Article

7.3 | Implications for phase equilibrium modelling

The phase diagrams (Figures 9a, 10a and 12) for the bulk rock and the melt pocket do not show a stable epidote-group mineral at UHP, but the calcic composition of the crystallized melt pockets and the lack of K-bearing phases argue for the former existence of an epidote-group mineral. Epidote melting would not occur on the path of exhumation with slight heating; the diagram predicts that modal epidote increases with cooling. Various factors can influence phase relations and accuracy of phase equilibrium modelling, for example, estimates of equilibrium composition (e.g. Lanari & Engi, 2017; Stüwe, 1997), solid solution models and mineral composition analysis (e.g. Palin, Weller, et al., 2016). Melt loss can also lead to inaccurate bulk rock composition for phase equilibrium modelling of the hand specimen. The *P*–*X*(CaO) phase diagram shows that a slightly higher amount of CaO (12.5 wt%) in the bulk composition stabilizes an epidote-group mineral at UHP. Melt loss causes the decrease of the component in the residual sample, which renders phase diagram modelled with such composition incorrect. All these factors contribute to uncertainties in quantitatively determining exact *P*–*T* conditions for the metamorphic stages.

Our phase diagram modelled with the bulk composition of the Verpenesset eclogite (Appendix S1 and Figure S1) shows a large discrepancy with experimental results; i.e., zoisite can exist up to 1400 ˚C at UHP in experiments on natural zoisite eclogites (Skjerlie & Patiño Douce, 2002), but the upper temperature limit of zoisite in modelled diagram is about 200 ˚C lower. The contradicting phase relations between models and experiments imply that large uncertainties still exist, particularly in the solid-solution models for the epidote-group mineral and melt. The model for epidote-group mineral needs to be improved, for example, by thermodynamic data on the incorporation of Fe^{3+} into pure endmembers of zoisite and clinozoisite (e.g. Enami, Liou, & Mattinson, 2004), on the basis of thermochemical measurements by experiments. The melt solution model needs to be further developed by extending applicability to higher *P* and producing more reliable results at UHP.

8 | SUMMARY AND CONCLUSION

The UHP kyanite eclogite from Rabbit Ears Island in North-East Greenland was partially melted at HP during exhumation. A peak mineral assemblage of garnet, omphacite, kyanite, coesite, rutile, clinozoisite, and former presence of phengite are documented in the kyanite eclogite. Numerous partial melting textures, such as cuspate grain boundaries, graphic intergrowths, neoblasts and polymineralic inclusions, reveal that the kyanite eclogite was partially melted. Abundant Ca-rich polymineralic assemblages of clinopyroxene, amphibole, plagioclase, peritectic garnet, with or without kyanite indicate that an epidote group mineral was the main melted phase. Phase equilibria demonstrate that the kyanite eclogite reached peak conditions of 3.4 GPa at 940 ˚C, which is located at subsolidus in both the modelled isochemical phase equilibrium diagrams and experiments for metabasites. Experimental phase relations revealed that a major melting event occurred at 2.2 GPa, 920 ˚C. Phase equilibria of a melt pocket shows that the partial melting continued to 1.4 GPa, 900 ˚C. The assemblage of amphibole, clinopyroxene and plagioclase in the symplectite after omphacite and the melt pocket equilibrated at 1.3 GPa, 717–732 ˚C. The problem of the modelled phase diagrams not agreeing with experimental phase relations is mainly attributed to uncertainties of the epidote and melt solution models.

ACKNOWLEDGEMENTS

The authors thank M. Brown for comments and editorial handling, and R. Palin and P. Lanari for their constructive reviews. We also thank T. Theye for his help with the electron microprobe analysis and valuable discussions. This study was supported by NSF grant EAR-1049433 to Gilotti. Cao appreciates the support of the Max and Lorraine Littlefield Research

This article is protected by copyright. All rights reserved.

Accepted Article

Fund from the Department of Earth and Environmental Sciences and the T. Anne Cleary Dissertation Research Fellowship from the Graduate College, the University of Iowa.

Accepted Article

REFERENCES

Bakker, R. J., & Elburg, M. A. (2006). A magmatic-hydrothermal transition in Arkaroola (northern Flinders Ranges, South Australia): from diopside–titanite pegmatites to hematite–quartz growth. *Contributions to Mineralogy and Petrology, 152*(5), 541-569. doi:10.1007/s00410-006-0125-0

Beaty, D., Hill, S., Albee, A., & Baldridge, W. (1979). *Apollo 12 feldspathic basalts 12031, 12038 and 12072-Petrology, comparison and interpretations.* Paper presented at the Lunar and Planetary Science Conference Proceedings.

Bigge, N., Martin, C., & Harlow, G. (2016). *PTX conditions of symplectite formation in the eclogites from the Western Gneiss Region (Norway).* Paper presented at the EGU General Assembly Conference Abstracts.

Brandelik, A. (2009). CALCMIN - an EXCEL (TM) Visual Basic application for calculating mineral structural formulae from electron microprobe analyses. *Computers & Geosciences, 35*(7), 1540-1551. doi:10.1016/j.cageo.2008.09.011

Braun, I., Raith, M., & Kumar, G. R. (1996). Dehydration-melting phenomena in leptynitic gneisses and the generation of leucogranites: a case study from the Kerala Khondalite Belt, southern India. *Journal of Petrology, 37*(6), 1285-1305.

Brey, G. P., & Köhler, T. (1990). Geothermobarometry in four-phase lherzolites II: New thermobarometers, and practical assessment of existing thermobarometers. *Journal of Petrology, 31*(6), 1353-1378.

Brown, M. (2001). Orogeny, migmatites and leucogranites: a review. *Journal of Earth System Science, 110*(4), 313-336.

Brown, M. (2007). Crustal melting and melt extraction, ascent and emplacement in orogens: mechanisms and consequences. *Journal of the Geological Society, 164*(4), 709-730. doi:10.1144/0016-76492006-171

Brueckner, H. K., Gilotti, J. A., & Nutman, A. P. (1998). Caledonian eclogite-facies metamorphism of Early Proterozoic protoliths from the North-East Greenland Eclogite Province. *Contributions to Mineralogy and Petrology, 130*, 103-120.

Caddick, M. J., Konopásek, J., & Thompson, A. B. (2010). Preservation of garnet growth zoning and the duration of prograde metamorphism. *Journal of Petrology, 51*(11), 2327-2347.

Cesare, B., Ferrero, S., Salviolo-Mariani, E., Pedron, D., & Cavallo, A. (2009). "Nanogranite" and glassy inclusions: The anatectic melt in migmatites and granulites. *Geology, 37*(7), 627-630. doi:10.1130/G25759a.1

Chen, D. L., Liu, L., Sun, Y., & Zhu, X. H. (2010). The retrograde partial melting of the Xitieshan UHP eclogite from the North Qaidam, NW China. *Geochimica Et Cosmochimica Acta, 74*(12), A167-A167.

Chen, Y. X., Zheng, Y. F., Gao, X. Y., & Hu, Z. (2014). Multiphase solid inclusions in zoisite-bearing eclogite: evidence for partial melting of ultrahigh-pressure metamorphic rocks during continental collision. *Lithos, 200*, 1-21. doi:10.1016/j.lithos.2014.04.004

Connolly, J. A. D. (2005). Computation of phase equilibria by linear programming: A tool for geodynamic modeling and its application to subduction zone decarbonation. *Earth and Planetary Science Letters, 236*(1-2), 524-541. doi:10.1016/j.epsl.2005.04.033

Diener, J. F. A., & Powell, R. (2010). Influence of ferric iron on the stability of mineral assemblages. *Journal of Metamorphic Geology, 28*(6), 599-613. doi:10.1111/j.1525-1314.2010.00880.x

This article is protected by copyright. All rights reserved.

Accepted Article

Diener, J. F. A., & Powell, R. (2012). Revised activity-composition models for clinopyroxene and amphibole. *Journal of Metamorphic Geology, 30*(2), 131-142. doi:10.1111/j.1525-1314.2011.00959.x

Ellis, D. J., & Green, D. H. (1979). An experimental study of the effect of Ca upon garnet-clinopyroxene Fe-Mg exchange equilibria. *Contributions to Mineralogy and Petrology, 71*(1), 13-22. doi:Doi 10.1007/Bf00371878

Elvevold, S., & Gilotti, J. A. (2000). Pressure-temperature evolution of retrogressed kyanite eclogites, Weinschenk Island, North-East Greenland Caledonides. *Lithos, 53*(2), 127-147. doi:Doi 10.1016/S0024-4937(00)00014-1

Enami, M., Liou, J. G., & Mattinson, C. G. (2004). Epidote minerals in high P/T metamorphic terranes: Subduction zone and high- to ultrahigh-pressure metamorphism. *Reviews in mineralogy and geochemistry, 56*(1), 347-398. doi:10.2138/gsrmg.56.1.347

Fenn, P. M. (1986). On the origin of graphic granite. *American Mineralogist, 71*(3-4), 325-330.

Ferrando, S., Frezzotti, M. L., Petrelli, M., & Compagnoni, R. (2009). Metasomatism of continental crust during subduction: the UHP whiteschists from the Southern Dora-Maira Massif (Italian Western Alps). *Journal of Metamorphic Geology, 27*(9), 739-756. doi:10.1111/j.1525-1314.2009.00837.x

Ferrero, S., Bartoli, O., Cesare, B., Salvioli-Mariani, E., Acosta-Vigil, A., Cavallo, A., . . . Battiston, S. (2012). Microstructures of melt inclusions in anatectic metasedimentary rocks. *Journal of Metamorphic Geology, 30*(3), 303-322. doi:10.1111/j.1525-1314.2011.00968.x

Frezzotti, M. L., & Ferrando, S. (2015). The chemical behavior of fluids released during deep subduction based on fluid inclusions. *American Mineralogist, 100*(2-3), 352-377. doi:10.2138/am-2015-4933

Fuhrman, M. L., & Lindsley, D. H. (1988). Ternary-feldspar modeling and thermometry. *American Mineralogist, 73*(3-4), 201-215.

Gao, X. Y., Zheng, Y. F., & Chen, Y. X. (2012). Dehydration melting of ultrahigh-pressure eclogite in the Dabie orogen: evidence from multiphase solid inclusions in garnet. *Journal of Metamorphic Geology, 30*(2), 193-212. doi:10.1111/j.1525-1314.2011.00962.x

Gao, X. Y., Zheng, Y. F., Chen, Y. X., & Hu, Z. (2014). Composite carbonate and silicate multiphase solid inclusions in metamorphic garnet from ultrahigh-P eclogite in the Dabie orogen. *Journal of Metamorphic Geology, 32*(9), 961-980. doi:10.1111/jmg.12102

Gilotti, J. A. (1993). Discovery of a medium-temperature eclogite province in the Caledonides of North-East Greenland. *Geology, 21*(6), 523-526. doi:Doi 10.1130/0091-7613(1993)021<0523:Doamte>2.3.Co;2

Gilotti, J. A., Jones, K. A., & Elvevold, S. (2008). Caledonian metamorphic patterns in Greenland. In A. K. Higgins, J. A. Gilotti, & M. P. Smith (Eds.), *The Greenland Caledonides: Evolution of the Northeast Margin of Laurentia* (Vol. 202, pp. 201-225): Geological Society of America Memoir.

Gilotti, J. A., & McClelland, W. C. (2007). Characteristics of, and a tectonic model for, ultrahigh-pressure metamorphism in the overriding plate of the Caledonian Orogen. *International Geology Review, 49*, 777-797.

Gilotti, J. A., & McClelland, W. C. (2011). Geochemical and geochronological evidence that the North-East Greenland ultrahigh-pressure terrane is Laurentian crust. *The Journal of Geology, 119*(5), 439-456. doi:10.1086/660867

This article is protected by copyright. All rights reserved.

Gilotti, J. A., McClelland, W. C., & Wooden, J. L. (2014). Zircon captures exhumation of an ultrahigh-pressure terrane, North-East Greenland Caledonides. *Gondwana Research, 25*(1), 235-256. doi:10.1016/j.gr.2013.03.018

Gilotti, J. A., Nutman, A. P., & Brueckner, H. K. (2004). Devonian to Carboniferous collision in the Greenland Caledonides: U-Pb zircon and Sm-Nd ages of high-pressure and ultrahigh-pressure metamorphism. *Contributions to Mineralogy and Petrology, 148*(2), 216-235. doi:10.1007/s00410-004-0600-4

Gilotti, J. A., & Ravna, E. J. K. (2002). First evidence for ultrahigh-pressure metamorphism in the North-East Greenland Caledonides. *Geology, 30*(6), 551-554. doi:10.1130/0091-7613(2002)030<0551:Fefupm>2.0.Co;2

Gottschalk, M. (2004). Thermodynamic properties of zoisite, clinozoisite and epidote. *Reviews in Mineralogy & Geochemistry, 56*, 83-124. doi:DOI 10.2138/gsrmg.56.1.83

Green, E. C. R., Holland, T. J. B., & Powell, R. (2007). An order-disorder model for omphacitic pyroxenes in the system jadeite-diopside-hedenbergite-acmite, with applications to eclogitic rocks. *American Mineralogist, 92*(7), 1181-1189. doi:10.2138/am.2007.2401

Green, E. C. R., White, R. W., Diener, J. F. A., Powell, R., Holland, T. J. B., & Palin, R. M. (2016). Activity-composition relations for the calculation of partial melting equilibria in metabasic rocks. *Journal of Metamorphic Geology, 34*, 845-869. doi:10.1111/jmg.12211

Groppo, C., & Castelli, D. (2010). Prograde P-T evolution of a lawsonite eclogite from the Monviso meta-ophiolite (Western Alps): Dehydration and redox reactions during subduction of oceanic FeTi-oxide gabbro. *Journal of Petrology, 51*(12), 2489-2514. doi:10.1093/petrology/egq065

Guiraud, M., Powell, R., & Rebay, G. (2001). H_2O in metamorphism and unexpected behaviour in the preservation of metamorphic mineral assemblages. *Journal of Metamorphic Geology, 19*(4), 445-454. doi:DOI 10.1046/j.0263-4929.2001.00320.x

Hacker, B. R., Kelemen, P. B., & Behn, M. D. (2011). Differentiation of the continental crust by relamination. *Earth and Planetary Science Letters, 307*(3-4), 501-516. doi:10.1016/j.epsl.2011.05.024

Hacker, B. R., Luffi, P., Lutkov, V., Minaev, V., Ratschbacher, L., Plank, T., . . . Metcalf, J. (2005). Near-ultrahigh pressure processing of continental crust: Miocene crustal xenoliths from the Pamir. *Journal of Petrology, 46*(8), 1661-1687.

Hallett, B. W., McClelland, W. C., & Gilotti, J. A. (2014). The timing of strike-slip deformation along the Storstrømmen shear zone, Greenland Caledonides: U-Pb zircon and titanite geochronology. *Geoscience Canada, 41*, 19-45.

Harley, S. L., & Green, D. H. (1982). Garnet ortho-pyroxene barometry for granulites and peridotites. *Nature, 300*(5894), 697-701. doi:DOI 10.1038/300697a0

Harte, B., Hunter, R., & Kinny, P. (1993). Melt geometry, movement and crystallization, in relation to mantle dykes, veins and metasomatism. *Philosophical Transactions of the Royal Society of London A: Mathematical, Physical and Engineering Sciences, 342*(1663), 1-21.

Hawthorne, F. C., Oberti, R., Harlow, G. E., Maresch, W. V., Martin, R. F., Schumacher, J. C., & Welch, M. D. (2012). Nomenclature of the amphibole supergroup. *American Mineralogist, 97*(11-12), 2031-2048. doi:10.2138/am.2012.4276

Hermann, J., & Rubatto, D. (2014). 4.9 - Subduction of continental crust to mantle depth: Geochemistry of ultrahigh-pressure rocks. In K. K. Turekian (Ed.), *Treatise on Geochemistry (Second Edition)* (pp. 309-340). Oxford: Elsevier.

This article is protected by copyright. All rights reserved.

Accepted Article

Accepted Article

Holland, T. J. B., & Blundy, J. (1994). Nonideal interactions in calcic amphiboles and their bearing on amphibole-plagioclase thermometry. *Contributions to Mineralogy and Petrology, 116*(4), 433-447. doi:10.1007/Bf00310910

Holland, T. J. B., & Powell, R. (2001). Calculation of phase relations involving haplogranitic melts using an internally consistent thermodynamic dataset. *Journal of Petrology, 42*(4), 673-683. doi:10.1093/petrology/42.4.673

Holland, T. J. B., & Powell, R. (2011). An improved and extended internally consistent thermodynamic dataset for phases of petrological interest, involving a new equation of state for solids. *Journal of Metamorphic Geology, 29*(3), 333-383. doi:10.1111/j.1525-1314.2010.00923.x

Holness, M. B. (2006). Melt–solid dihedral angles of common minerals in natural rocks. *Journal of Petrology, 47*(4), 791-800.

Holness, M. B., Cesare, B., & Sawyer, E. W. (2011). Melted rocks under the microscope: Microstructures and their interpretation. *Elements, 7*(4), 247-252. doi:10.2113/gselements.7.4.247

Holness, M. B., & Sawyer, E. W. (2008). On the Pseudomorphing of Melt-filled Pores During the Crystallization of Migmatites. *Journal of Petrology, 49*(7), 1343-1363. doi:10.1093/petrology/egn028

Hwang, S.-L., Shen, P., Chu, H.-T., Yui, T.-F., Liou, J. G., Sobolev, N. V., & Shatsky, V. S. (2005). Crust-derived potassic fluid in metamorphic microdiamond. *Earth and Planetary Science Letters, 231*(3), 295-306.

Joanny, V., Vanroermund, H., & Lardeaux, J. M. (1991). The clinopyroxene plagioclase symplectite in retrograde eclogites: a potential geothermobarometer. *Geologische Rundschau, 80*(2), 303-320. doi:Doi 10.1007/Bf01829368

Jurewicz, S. R., & Watson, E. B. (1984). Distribution of partial melt in a felsic system: the importance of surface energy. *Contributions to Mineralogy and Petrology, 85*(1), 25-29.

Kalsbeek, F., Thrane, K., Higgins, A. K., Jepsen, H. F., Leslie, A. G., Nutman, A. P., & Frei, R. (2008). Polyorogenic history of the East Greenland Caledonides. In A. K. Higgins, J. A. Gilotti, & M. P. Smith (Eds.), *The Greenland Caledonides: Evolution of the Northeast Margin of Laurentia* (pp. 55-72). The Geological Society of America Memoir 202.

Kessel, R., Ulmer, P., Pettke, T., Schmidt, M. W., & Thompson, A. B. (2005). The water-basalt system at 4 to 6 GPa: Phase relations and second critical endpoint in a K-free eclogite at 700 to 1400 degrees C. *Earth and Planetary Science Letters, 237*(3-4), 873-892. doi:10.1016/j.epsl.2005.06.018

Kriegsman, L. M. (2001). Partial melting, partial melt extraction and partial back reaction in anatectic migmatites. *Lithos, 56*(1), 75-96. doi:Doi 10.1016/S0024-4937(00)00060-8

Labrousse, L., Prouteau, G., & Ganzhorn, A. C. (2011). Continental exhumation triggered by partial melting at ultrahigh pressure. *Geology, 39*(12), 1171-1174. doi:10.1130/G32316.1

Lanari, P., & Engi, M. (2017). Local bulk composition effects on metamorphic mineral assemblages. *Reviews in mineralogy and geochemistry, 83*(1), 55-102.

Lang, H. M., & Gilotti, J. A. (2007). Partial melting of metapelites at ultrahigh-pressure conditions, Greenland Caledonides. *Journal of Metamorphic Geology, 25*(2), 129-147. doi:10.1111/j.1525-1314.2006.00687.x

Lang, H. M., & Gilotti, J. A. (2015). Modeling the exhumation path of partially melted ultrahigh-pressure metapelites, North-East Greenland Caledonides. *Lithos, 226*, 131-146. doi:10.1016/j.lithos.2014.10.010

This article is protected by copyright. All rights reserved.

Laporte, D., Rapaille, C., & Provost, A. (1997). Wetting angles, equilibrium melt geometry, and the permeability threshold of partially molten crustal protoliths *Granite: from segregation of melt to emplacement fabrics* (pp. 31-54): Springer.

Lentz, D. R., & Fowler, A. D. (1992). A dynamic model for graphic quartz-feldspar intergrowths in granitic pegmatites in the southwestern Grenville Province. *Canadian Mineralogist, 30*(3), 571-585.

Liu, F. L., Robinson, P. T., & Liu, P. H. (2012). Multiple partial melting events in the Sulu UHP terrane: zircon U–Pb dating of granitic leucosomes within amphibolite and gneiss. *Journal of Metamorphic Geology, 30*(8), 887-906. doi:10.1111/j.1525-1314.2012.01005.x

Liu, P. L., Wu, Y., Liu, Q., Zhang, J. F., Zhang, L., & Jin, Z. M. (2014). Partial melting of UHP calc-gneiss from the Dabie Mountains. *Lithos, 192*, 86-101. doi:10.1016/j.lithos.2014.01.012

Liu, Q., Hermann, J., & Zhang, J. F. (2013). Polyphase inclusions in the Shuanghe UHP eclogites formed by subsolidus transformation and incipient melting during exhumation of deeply subducted crust. *Lithos, 177*, 91-109. doi:10.1016/j.lithos.2013.06.010

Liu, Q., Jin, Z. M., & Zhang, J. F. (2009). An experimental study of dehydration melting of phengite-bearing eclogite at 1.5-3.0 GPa. *Chinese Science Bulletin, 54*(12), 2090-2100. doi:10.1007/s11434-009-0140-4

Liu, Q., & Wu, Y. (2013). Dehydration melting of UHP eclogite and paragneiss in the Dabie orogen: Evidence from laboratory experiment to natural observation. *Chinese Science Bulletin, 58*(35), 4390-4396. doi:10.1007/s11434-013-6075-9

Locock, A. J. (2014). An Excel spreadsheet to classify chemical analyses of amphiboles following the IMA 2012 recommendations. *Computers & Geosciences, 62*, 1-11. doi:10.1016/j.cageo.2013.09.011

London, D., & Morgan, G. B. (2012). The pegmatite puzzle. *Elements, 8*(4), 263-268.

Longhi, J., & Jurewicz, S. (1995). *Plagioclase-melt wetting angles and textures: implications for anorthosites.* Paper presented at the Lunar and Planetary Science Conference.

Marmo, B. A., Clarke, G. L., & Powell, R. (2002). Fractionation of bulk rock composition due to porphyroblast growth: effects on eclogite facies mineral equilibria, Pam Peninsula, New Caledonia. *Journal of Metamorphic Geology, 20*(1), 151-165. doi:10.1046/j.0263-4929.2001.00346.x

Martin, C. (2018). P-T conditions of symplectite formation in the eclogites from the Western Gneiss Region (Norway). In S. Ferrero, P. Lanari, P. Goncalves, & E. G. Grosch (Eds.), *Metamorphic Geology: Microscale to Mountain Belts* (Vol. 478): Geological Society, London, Special Publications.

Martin, C., & Duchene, S. (2015). Residual water in hydrous minerals as a kinetic factor for omphacite destabilization into symplectite in the eclogites of Vardalsneset (WGR, Norway). *Lithos, 232*, 162-173. doi:10.1016/j.lithos.2015.06.021

Massonne, H.-J. (2012). Formation of amphibole and clinozoisite-epidote in eclogite owing to fluid infiltration during exhumation in a subduction channel. *Journal of Petrology, 53*(10), 1969-1998. doi:10.1093/petrology/egs040

Massonne, H.-J. (2013). Constructing the pressure-temperature path of ultrahigh-pressure rocks. *Elements, 9*(4), 267-272. doi:10.2113/gsetements.9.4.267

Massonne, H.-J. (2014). Wealth of P-T-t information in medium-high grade metapelites: Example from the Jubrique Unit of the Betic Cordillera, S Spain. *Lithos, 208*, 137-157. doi:10.1016/j.lithos.2014.08.027

This article is protected by copyright. All rights reserved.

Accepted Article

Massonne, H.-J. (2015). Derivation of P-T paths from high-pressure metagranites - Examples from the Gran Paradiso Massif, western Alps. *Lithos, 226*, 265-279. doi:10.1016/j.lithos.2014.12.024

Massonne, H.-J., & Fockenberg, T. (2015). *Melting of eclogite at ultrahigh-pressure (UHP) conditions: an experimental study.* Paper presented at the International Eclogite Conference, Domincan Republic.

Mattinson, C. G., Zhang, R. Y., Tsujimori, T., & Liou, J. G. (2004). Epidote-rich talc-kyanite-phengite eclogites, Sulu terrane, eastern China: P-T-f(O2) estimates and the significance of the epidote-talc assemblage in eclogite. *American Mineralogist, 89*(11-12), 1772-1783.

McClelland, W. C., Gilotti, J. A., Mazdab, F. K., & Wooden, J. L. (2009). Trace-element record in zircons during exhumation from UHP conditions, North-East Greenland Caledonides. *European Journal of Mineralogy, 21*(6), 1135-1148. doi:10.1127/0935-1221/2009/0021-2000

McClelland, W. C., Gilotti, J. A., Ramarao, T., Stemmerik, L., & Dalhoff, F. (2016). Carboniferous basin in Holm Land records local exhumation of the North-East Greenland Caledonides: Implications for the detrital zircon signature of a collisional orogen. *Geosphere, 12*(3), 925 - 947. doi:10.1130/ges01284.1

McClelland, W. C., Power, S. E., Gilotti, J. A., & Mazdab, F. K. (2006). U-Pb SHRIMP geochronology and trace-element geochemistry of coesite-bearing zircons, North-East Greenland Caledonides. In B. R. Hacker, W. C. McClelland, & J. G. Liou (Eds.), *Ultrahigh-Pressure Metamorphism: Deep Continental Subduction* (pp. 23-43): The Geological Society of America Special Paper 403.

Mottana, A., Rossi, G., Kracher, A., & Kurat, G. (1979). Violan revisited: Mn-bearing omphacite and diopside. *Tschermaks mineralogische und petrographische Mitteilungen, 26*(3), 187-201. doi:10.1007/bf01081845

Nestola, F., Merli, M., Nimis, P., Parisatoo, M., Kopylova, M., De Stefano, A., . . . Manghnani, M. (2012). In situ analysis of garnet inclusion in diamond using single-crystal X-ray diffraction and X-ray micro-tomography. *European Journal of Mineralogy, 24*(4), 599-606. doi:10.1127/0935-1221/2012/0024-2212

Nijland, T. G., & Touret, J. L. (2001). Replacement of graphic pegmatite by graphic albite-actinolite-clinopyroxene intergrowths (Mjåvatn, southern Norway). *European Journal of Mineralogy, 13*(1), 41-50.

Oberti, R., Ungaretti, L., Cannillo, E., Hawthorne, F. C., & Memmi, I. (1995). Temperature-dependent Al order-disorder in the tetrahedral double chain of C2/m amphiboles. *European Journal of Mineralogy, 7*(5), 1049-1063.

Palin, R. M., St-Onge, M. R., Waters, D. J., Searle, M. P., & Dyck, B. (2014). Phase equilibria modelling of retrograde amphibole and clinozoisite in mafic eclogite from the Tso Morari massif, northwest India: constraining the P-T-M(H2O) conditions of exhumation. *Journal of Metamorphic Geology, 32*(7), 675-693. doi:10.1111/jmg.12085

Palin, R. M., Weller, O. M., Waters, D. J., & Dyck, B. (2016). Quantifying geological uncertainty in metamorphic phase equilibria modelling; a Monte Carlo assessment and implications for tectonic interpretations. *Geoscience Frontiers, 7*(4), 591-607. doi:http://dx.doi.org/10.1016/j.gsf.2015.08.005

Palin, R. M., White, R. W., & Green, E. C. R. (2016). Partial melting of metabasic rocks and the generation of tonalitic–trondhjemitic–granodioritic (TTG) crust in the Archaean: Constraints from phase equilibrium modelling. *Precambrian Research, 287*, 73-90. doi:http://dx.doi.org/10.1016/j.precamres.2016.11.001

This article is protected by copyright. All rights reserved.

Accepted Article

Accepted Article

Perchuk, A. L., Burchard, M., Maresch, W. V., & Schertl, H. P. (2008). Melting of hydrous and carbonate mineral inclusions in garnet host during ultrahigh pressure experiments. *Lithos, 103*(1-2), 25-45. doi:10.1016/j.lithos.2007.09.008

Perchuk, A. L., Davydova, V. V., Burchard, M., Maresch, W. V., Schertl, H. P., Yapaskurt, V. O., & Safonov, O. G. (2009). Modification of mineral inclusions in garnet under high-pressure conditions: experimental simulation and application to the carbonate-silicate rocks of Kokchetav massif. *Russian Geology and Geophysics, 50*(12), 1153-1168. doi:10.1016/j.rgg.2009.11.014

Petrie, M. B., Massonne, H.-J., Gilotti, J. A., McClelland, W. C., & Van Staal, C. (2016). The P–T path of eclogites in the St. Cyr klippe, Yukon, Canada: Permian metamorphism of a coherent high-pressure unit in an accreted terrane of the North American Cordillera. *European Journal of Mineralogy*. doi:10.1127/ejm/2016/0028-2576

Phillipsi, M., Colville, A., & Ribbe, P. (1971). The crystal structures of two oligoclases: A comparison with low and high albite. *Zeitschrift für Kristallographie-Crystalline Materials, 133*(1-6), 43-65.

Poli, S., & Schmidt, M. W. (2004). Experimental subsolidus studies on epidote minerals. *Epidotes, 56*, 171-195. doi:10.2138/gsrmg.56.1.171

Powell, R., Holland, T., & Worley, B. (1998). Calculating phase diagrams involving solid solutions via non-linear equations, with examples using THERMOCALC. *Journal of Metamorphic Geology, 16*(4), 577-588. doi:DOI 10.1111/j.1525-1314.1998.00157.x

Rapp, R. P., & Watson, E. B. (1995). Dehydration melting of metabasalt at 8-32 Kbar: Implications for continental growth and crust-mantle recycling. *Journal of Petrology, 36*(4), 891-931.

Rapp, R. P., Watson, E. B., & Miller, C. F. (1991). Partial melting of amphibolite eclogite and the origin of Archean trondhjemites and tonalites. *Precambrian Research, 51*(1-4), 1-25. doi:Doi 10.1016/0301-9268(91)90092-O

Ravna, E. J. K., & Terry, M. P. (2004). Geothermobarometry of UHP and HP eclogites and schists - an evaluation of equilibria among garnet-clinopyroxene-kyanite-phengite-coesite/quartz. *Journal of Metamorphic Geology, 22*(6), 579-592. doi:10.1111/j.1525-1314.2004.00534.x

Rosenberg, C., & Handy, M. (2005). Experimental deformation of partially melted granite revisited: implications for the continental crust. *Journal of Metamorphic Geology, 23*(1), 19-28.

Rosenberg, C., & Riller, U. (2000). Partial-melt topology in statically and dynamically recrystallized granite. *Geology, 28*(1), 7-10.

Sawyer, E. (2001). Melt segregation in the continental crust: distribution and movement of melt in anatectic rocks. *Journal of Metamorphic Geology, 19*(3), 291-309.

Schmidt, M. W., & Poli, S. (2014). Devolatilization during subduction. In H. D. Holland & K. K. Turekian (Eds.), *Treatise on Geochemistry (Second Edition)* (Vol. 4, pp. 669-701). Oxford: Elsevier.

Schmidt, M. W., Vielzeuf, D., & Auzanneau, E. (2004). Melting and dissolution of subducting crust at high pressures: the key role of white mica. *Earth and Planetary Science Letters, 228*(1-2), 65-84. doi:10.1016/j.epsl.2004.09.020

Shatsky, V. S., Jagoutz, E., Sobolev, N. V., Kozmenko, O. A., Parkhomenko, V. S., & Troesch, M. (1999). Geochemistry and age of ultrahigh pressure metamorphic rocks from the Kokchetav massif (Northern Kazakhstan). *Contributions to Mineralogy and Petrology, 137*(3), 185-205. doi:10.1007/s004100050545

Skjerlie, K. P., & Patiño Douce, A. E. (2002). The fluid-absent partial melting of a zoisite-bearing quartz eclogite from 1.0 to 3.2 GPa: Implications for melting in thickened

This article is protected by copyright. All rights reserved.

continental crust and for subduction-zone processes. *Journal of Petrology, 43*(2), 291-314. doi:10.1093/petrology/43.2.291
Smith, J. V. (2012). *Feldspar Minerals: 2 Chemical and Textural Properties*: Springer Science & Business Media.
Spruzeniece, L., Piazolo, S., Daczko, N. R., Kilburn, M. R., & Putnis, A. (2016). Symplectite formation in the presence of a reactive fluid: insights from hydrothermal experiments. *Journal of Metamorphic Geology*, 281-299. doi:10.1111/jmg.12231
Stüwe, K. (1997). Effective bulk composition changes due to cooling: a model predicting complexities in retrograde reaction textures. *Contributions to Mineralogy and Petrology, 129*(1), 43-52. doi:10.1007/s004100050322
Tedeschi, M., Lanari, P., Rubatto, D., Pedrosa-Soares, A., Hermann, J., Dussin, I., . . . Baumgartner, L. (2017). Reconstruction of multiple P-T-t stages from retrogressed mafic rocks: Subduction versus collision in the Southern Brasília orogen (SE Brazil). *Lithos, 294*, 283-303.
Tinkham, D. K., Zuluaga, C. A., & Stowell, H. H. (2001). Metapelite phase equilibria modeling in MnNCKFMASH: The effect of variable Al_2O_3 and MgO/(MgO+FeO) on mineral stability. *Geological Materials Research, 3*(1), 1-42.
Tomkins, H. S., Powell, R., & Ellis, D. J. (2007). The pressure dependence of the zirconium-in-rutile thermometer. *Journal of Metamorphic Geology, 25*(6), 703-713. doi:10.1111/j.1525-1314.2007.00724.x
Vernon, R. H. (2004). *A practical guide to rock microstructure*: Cambridge university press.
Vielzeuf, D., & Schmidt, M. W. (2001). Melting relations in hydrous systems revisited: application to metapelites, metagreywackes and metabasalts. *Contributions to Mineralogy and Petrology, 141*(3), 251-267.
Wade, J., Dyck, B., Palin, R. M., Moore, J. D. P., & Smye, A. J. (2017). The divergent fates of primitive hydrospheric water on Earth and Mars. *Nature, 552*, 391. doi:10.1038/nature25031
Wang, L., Kusky, T. M., Polat, A., Wang, S. J., Jiang, X. F., Zong, K. Q., . . . Fu, J. M. (2014). Partial melting of deeply subducted eclogite from the Sulu orogen in China. *Nature Communications, 5*, 5604. doi:10.1038/ncomms6604
Wang, S. J., Wang, L., Brown, M., Piccoli, P. M., Johnson, T. E., Feng, P., . . . Huang, Y. (2017). Fluid generation and evolution during exhumation of deeply subducted UHP continental crust: Petrogenesis of composite granite–quartz veins in the Sulu belt, China. *Journal of Metamorphic Geology, 35*(6), 601-629. doi:doi:10.1111/jmg.12248
Watson, E. B., Wark, D. A., & Thomas, J. B. (2006). Crystallization thermometers for zircon and rutile. *Contributions to Mineralogy and Petrology, 151*(4), 413-433. doi:10.1007/s00410-006-0068-5
Weinberg, R. F., & Hasalova, P. (2015). Water-fluxed melting of the continental crust: A review. *Lithos, 212*, 158-188. doi:10.1016/j.lithos.2014.08.021
White, R. W., Powell, R., & Clarke, G. L. (2002). The interpretation of reaction textures in Fe-rich metapelitic granulites of the Musgrave Block, central Australia: constraints from mineral equilibria calculations in the system K_2O-FeO-MgO-Al_2O_3-SiO_2-H_2O-TiO_2-Fe_2O_3. *Journal of Metamorphic Geology, 20*(1), 41-55. doi:10.1046/j.0263-4929.2001.00349.x
White, R. W., Powell, R., Holland, T. J. B., Johnson, T. E., & Green, E. C. R. (2014). New mineral activity-composition relations for thermodynamic calculations in metapelitic systems. *Journal of Metamorphic Geology, 32*(3), 261-286. doi:10.1111/jmg.12071
White, R. W., Powell, R., Holland, T. J. B., & Worley, B. A. (2000). The effect of TiO_2 and Fe_2O_3 on metapelitic assemblages at greenschist and amphibolite facies conditions:

This article is protected by copyright. All rights reserved.

mineral equilibria calculations in the system K_2O-FeO-MgO-Al_2O_3-SiO_2-H_2O-TiO_2-Fe_2O_3. *Journal of Metamorphic Geology, 18*(5), 497-511.
Zack, T., Moraes, R., & Kronz, A. (2004). Temperature dependence of Zr in rutile: empirical calibration of a rutile thermometer. *Contributions to Mineralogy and Petrology, 148*(4), 471-488. doi:10.1007/s00410-004-0617-8
Zeng, L., Liang, F., Asimow, P., Chen, F., & Chen, J. (2009). Partial melting of deeply subducted continental crust and the formation of quartzofeldspathic polyphase inclusions in the Sulu UHP eclogites. *Chinese Science Bulletin, 54*(15), 2580-2594.
Zhao, Z.-F., Zheng, Y.-F., Wei, C.-S., & Wu, Y.-B. (2007). Post-collisional granitoids from the Dabie orogen in China: Zircon U–Pb age, element and O isotope evidence for recycling of subducted continental crust. *Lithos, 93*(3–4), 248-272. doi:http://dx.doi.org/10.1016/j.lithos.2006.03.067
Zheng, Y.-F., Xia, Q.-X., Chen, R.-X., & Gao, X.-Y. (2011). Partial melting, fluid supercriticality and element mobility in ultrahigh-pressure metamorphic rocks during continental collision. *Earth-Science Reviews, 107*(3-4), 342-374. doi:10.1016/j.earscirev.2011.04.004
Zuluaga, C. A., Stowell, H. H., & Tinkham, D. K. (2005). The effect of zoned garnet on metapelite pseudosection topology and calculated metamorphic P-T paths. *American Mineralogist, 90*(10), 1619-1628. doi:10.2138/am.2005.1741

SUPPLEMENTARY INFORMATION

Appendix S1.
Isochemical phase equilibrium diagram for zoisite eclogite in Skjerlie and Patiño Douce (2002).
Table S1. Whole rock bulk composition of zoisite eclogite in experiments by Skjerlie and Patiño Douce (2002) and adjusted for phase equilibrium modelling.
Figure S1. *P–T* phase diagram (A) of zoisite eclogite in experiments by Skjerlie and Patiño Douce (2002).

FIGURE AND TABLE CAPTIONS

Figure 1. a) Location of the ultrahigh-pressure (UHP) terrane on Rabbit Ears Island (REI) in the larger North-East Greenland eclogite province (NEGEP). b) Geological map of REI, modified after McClelland et al. (2006). c) Detailed geological map of the outcrop where 03-110 was collected, showing the field relations of eclogite boudins with respect to host gneisses and pegmatite. Location of pegmatite 03-111 studied by Gilotti et al. (2014) (G 14) and Gilotti and McClelland (2007) (GM 07) is also shown.
Figure 2. a) UHP kyanite eclogite with intrafolial folds of compositional layering; location of the kyanite eclogite 03-110. Hammer shaft is 50 cm. b) Image of small, interconnected felsic veins in foliated eclogite, with a field notebook for scale.
Figure 3. Photomicrographs showing retrograde textures in kyanite eclogite 03-110. A, E and F are under plane-polarized light (PPL); B–D are under cross-polarized light (XPL). A: Rare clinozoisite (Cz) is surrounded by amphibole (Amp) and plagioclase (Pl). B: Plagioclase is intergrown with biotite (Bt) and embays omphacite (Cpx I), as marked by arrows. C: Plagioclase surrounds kyanite (Ky I) and shows embayments into omphacite (pointed by the arrow). D: Graphic intergrowth of euhedral amphibole and poikiloblastic plagioclase; note the crystallographic orientation of amphibole is the same. E: Second generation, smaller garnet (Grt II at filled arrows) at the rim of the first generation garnet (Grt I). F: Garnet II with straight boundaries (filled arrows) against plagioclase. Note the plagioclase poikiloblast

This article is protected by copyright. All rights reserved.

in the upper part of the image, and string of bead of plagioclase in the box. The unfilled arrows in E-F point to a highly cuspate plagioclase.

Figure 4. Photomicrographs showing polymineralic inclusions in large garnet (Grt I) in the studied kyanite eclogites. A: Backscattered electron (BSE) image of a polymineralic inclusion of albite (Ab) and K-feldspar (Kfs). B: Polymineralic inclusion of quartz rimmed by clinopyroxene (Cpx II) + plagioclase (Pl). Plagioclase displays cuspate shapes at quartz (Qz)–Cpx II and Cpx II–Grt I boundaries, XPL. C: BSE image of polymineralic inclusion of quartz surrounded by clinopyroxene (Cpx II) and plagioclase. D. Polymineralic inclusion (connected to matrix) consisting of quartz, clinopyroxene (Cpx II), kyanite (Ky II) and plagioclase with magmatic texture (interstitial plagioclase and Cpx II). The filled arrow points to a euhedral crystal face of garnet against plagioclase. The unfilled arrows point to plagioclase cusps with low dihedral angles in garnet, XPL.

Figure 5. Major element X-ray maps of garnet I (A–D) and a compositional zoning profile in sample 03-110. Unit for the colour scale is marked as counts per time unit during EMP mapping. The black line on A marks the profile shown in E. E: Zoning profiles plotted with the left axis for almandine, pyrope and grossular and the right axis for spessartine.

Figure 6. Major element X-ray maps of Grt II, with colour scale as counts per time unit. Grt II is smaller than garnet I, and displays a composition similar to the rim of Grt I. The clinopyroxene grain (Cpx II) contains a higher Ca and Mg content at rim than the centre. Note the prominent cusps formed among plagioclase–garnet–garnet or plagioclase–garnet–clinopyroxene, marked by the arrows.

Figure 7. P–$X(H_2O)$ phase diagram for kyanite eclogite 03-110 modelled at 900 ˚C. The bulk composition used in the modeling varies from Na_2O 2.881, MgO 7.449, Al_2O_3 20.335, SiO_2 52.021, K_2O 0.119, CaO 11.136, TiO_2 0.293, MnO 0.098, FeO 5.635, O_2 0.031, H_2O 0.000 to Na_2O 2.852, MgO 7.376, Al_2O_3 20.132, SiO_2 51.501, K_2O 0.119, CaO 11.025, TiO_2 0.290, MnO 0.097, FeO 5.635, O_2 0.031, H_2O 1.000, all in weight percentages. A: P-$X(H_2O)$ diagram with water content varying from 0 ($X(H_2O) = 0$) to 1 wt% ($X(H_2O) = 1$). Phengite is the only hydrous mineral present in the peak assemblage at 900 ºC; epidote-group minerals are absent in the diagram. B. Modal amounts of melt and amphibole on the diagram. Modal melt increases with increasing water content; modal amphibole remains constant in amphibole-present fields, and increases with increasing water content in melt-absent fields.

Figure 8. P–X(CaO) diagram for kyanite eclogite 03-110 modelled at 900 ˚C. The bulk composition in wt% varies from Na_2O 2.908, MgO 7.519, Al_2O_3 20.527, SiO_2 52.511, K_2O 0.120, CaO 10.000, TiO_2 0.296, MnO 0.099, FeO 5.689, O_2 0.032, H_2O 0.300 to Na_2O 2.746, MgO 7.100, Al_2O_3 19.382, SiO_2 49.584, K_2O 0.114, CaO 15.000, TiO_2 0.279, MnO 0.093, FeO 5.371, O_2 0.030, H_2O 0.300. A: Phase diagram showing the influence of CaO content from 10 (corresponding to X(CaO) = 0) to 15 wt% CaO (X(CaO) = 1). The phase diagram shows that the upper stability limit of epidote increases with increasing CaO content. B: Isopleths of X_{Gr}-in-garnet and modal epidote on the P–X(CaO) phase diagram. X_{Gr}-in-garnet mostly depends on the bulk CaO content in the feldspar- and epidote-absent fields, and becomes more pressure-dependent in the feldspar-present and epidote-present fields.

Figure 9. P–T diagram for the kyanite eclogite. The bulk composition is given in Table 3. A: P–T isochemical phase equilibrium diagram with mineral assemblages labelled. The solidus, free fluid and epidote phase stability boundaries, and the quartz/coesite transformation are highlighted. The mineral assemblages saturated with a trace amount of water are above the curve marked by +V. B: Isopleths of X_{Alm}, X_{Gr} and X_{Py} in garnet for the diagram. C: Isopleths of X_{Jd}-in-Cpx, where Cpx refers to both Na-poor clinopyroxene and omphacite, and garnet, melt and epidote modes for the phase diagram.

Figure 10. P–T diagram for a crystallized melt domain (Figure 6); Table 3 gives the bulk composition. A: Isochemical phase equilibrium diagram showing phase relations of minerals.

This article is protected by copyright. All rights reserved.

Phase boundaries of melt, amphibole and epidote are highlighted. B: Isopleths of X_{Alm}, X_{Py}, and X_{Gr} in garnet (Grt II) for the phase diagram. The star marks where the *P–T* conditions are indicated by garnet isopleths. C: Isopleths of the X_{Ab}-in-Pl and X_{Jd}-in-Cpx. The star marks where the X_{Jd} and X_{Ab} contours intersect.

Figure 11. *P–T* diagram for a symplectite of amphibole, clinopyroxene and plagioclase after omphacite in the kyanite eclogite. See Table 3 for the bulk composition. A: *P–T* phase diagram showing the modeled phase relations. B: Isopleths of Ca in amphibole, and X_{Ab}-in-plagioclase and X_{Jd}-in-clinopyroxene in the modeled phase diagram. The star marks the *P–T* condition where the analyzed composition intersects.

Figure 12. Estimated *P–T* path (solid curve) for kyanite eclogite 03-110 along with modeled phase boundaries, and experimental and theoretical phase relations. The solid black line represents the wet solidus for a MORB (Mid-Ocean Ridge Basalt) from Kessel et al. (2005; K05). The gray dot-dashed curves of phengite-out and solidus are from Q. Liu et al. (2009), an experimental study on phengite- and zoisite-bearing eclogites. The thin dashed curve marks the solidus from experimental study on natural zoisite eclogite from Skjerlie and Patiño Douce (2002; SPD02). In the lower pressure region, theoretically derived epidote and amphibole breakdown melting of metabasites are shown (Vielzeuf and Schmidt, 2001; VS01): zoisite is present at < 790 ˚C and melted at higher temperature at < 2.5 GPa, while the grey area marks the multivariant field of amphibole+quartz breakdown. The exhumation path for the Northeast-Greenland UHP metapelites from Lang and Gilotti (2015) is marked as a thick closely-spaced dashed curve (LG15). Dashed and solid arrowed curves are deduced metamorphic *P–T* path of the studied UHP eclogite, with stars referring to estimated *P–T* conditions based on phase equilibria and empirical thermobarometry.

Table 1. Sequence of the metamorphic minerals from sample 03-110. The black lines on the table mark the presence of the minerals.

Table 2. Representative analyses of peak and retrograde mineral assemblages of sample 03-110 in textural settings. MP stands for crystallized melt pocket. FeO_{TOT} refers to total FeO. The dash symbol marks the elements that were not analyzed with the microprobe. Garnet is normalized to 24 oxygen atoms with 10 six- and eight-fold coordinated cations. Omphacite is normalized to 6 oxygen atoms with 4 cations. Plagioclase is normalized to 8 oxygen atoms; biotite is normalized to 11 oxygen. Amphibole is normalized to 24 anions, with Fe^{3+} estimated by charge balance.

Table 3. Analyzed bulk composition and adjusted and calculated compositions used for phase equilibrium modelling, all in weight % of oxides.

For online SI items:

Supinfo.pdf
Description

Appendix S1.

Isochemical phase equilibrium diagram for zoisite eclogite in Skjerlie and Patiño Douce (2002).

Table S1. Whole rock bulk composition of zoisite eclogite in experiments by Skjerlie and Patiño Douce (2002) and adjusted for phase equilibrium modelling.

Figure S1. *P–T* phase diagram (A) of zoisite eclogite in experiments by Skjerlie and Patiño Douce (2002).

This article is protected by copyright. All rights reserved.

Accepted Article

Accepted Article

Table 1.

	Prograde	Peak	Melting/crystallization	Retrograde
Garnet	———	———	———	
Clinopyroxene	———	———	———	———
Kyanite	———	———	———	———
Coesite		———		
Quartz	———		———	———
Phengite	———	———	———	
Epidote mineral	———	———	———	
Amphibole	———		———	———
Biotite	———		———	———
K-feldspar			———	———
Plagioclase	———		———	———
Rutile	———	———	———	———

This article is protected by copyright. All rights reserved.

Table 2. Representative analyses of peak and retrograde mineral assemblages of sample 03-110 in textural settings.

Miner	Grt			Omp	Grt II	Pl			Cpx II			Amp		Bt
Comm	Core	Inner	Outer	Matri	Rim	MP	Symplectite		MP	Symplectite		MP		
Analys	g1bl22	g1bl3	g1bl2	43	G-B19	G-B20	g1b-62	g1b-	G-B11	g1b-26	g1b-66	g1b-22	G-B17	m11
SiO_2	39.94	39.74	40.24	53.83	40.06	61.63	60.03	###	52.01	54.37	52.73	45.74	45.47	37.86
TiO_2	0.05	0.04	0.03	0.17	0.02	0.00	0.06	0.03	0.29	0.10	0.22	0.78	0.54	1.95
Al_2O_3	23.16	23.09	23.31	12.00	22.98	24.38	23.33	###	9.16	5.42	5.31	11.71	12.23	17.66
FeO_{TOT}	12.95	16.50	16.68	3.21	18.61	0.21	0.44	0.57	4.06	3.66	4.32	7.99	7.85	8.30
MnO	0.30	0.43	0.55	0.00	0.50	0.01	0.05	0.00	0.02	0.00	0.09	0.00	0.04	0.05
MgO	9.88	9.99	9.14	9.27	10.40	0.01	1.19	2.05	11.87	13.11	14.49	15.99	16.64	18.75
CaO	14.06	11.05	10.15	14.79	8.94	5.72	6.88	6.96	20.36	20.69	20.86	12.23	12.07	0.04
Na_2O	0.00	0.02	0.01	5.63	0.01	8.30	7.65	7.31	2.48	2.46	1.50	1.78	1.98	0.17
K_2O	-	-	-	0.00	-	0.18	0.29	0.30	0.00	0.05	0.12	0.83	0.58	10.42
Cr_2O_3	0.09	0.08	0.08	0.08	0.21	-	0.03	0.05	-	0.21	0.17	0.25	-	0.24
Total	100.44	100.94	100.19	98.98	101.73	100.44	99.95	99.42	100.25	100.07	99.81	97.30	97.40	95.44
No Oxyge	24	24	24	6	24	8	8	8	6	6	6			11
Si	5.85	5.82	6.05	1.93	5.86	2.73	2.69	2.68	1.88	1.97	1.92	6.58	6.45	2.74
Ti	0.01	0.00	0.00	0.00	0.00	0.00	0.00	0.00	0.01	0.00	0.01	0.08	0.06	0.11
Al	4.00	3.99	4.13	0.51	3.96	1.27	1.23	1.20	0.39	0.23	0.23	1.99	2.04	1.51
Fe_{3+}	0.00	0.00	0.00	0.01	0.01	0.00	0.02	0.02	0.01	0.00	0.03	0.11	0.63	0.00
Fe_{2+}	1.59	2.02	2.10	0.09	2.27	0.01	0.00	0.00	0.11	0.11	0.10	0.07	0.30	0.50
Mn	0.04	0.05	0.07	0.00	0.06	0.00	0.00	0.00	0.00	0.00	0.00	0.01	0.01	0.00
Mg	2.16	2.18	2.05	0.50	2.27	0.00	0.00	0.00	0.64	0.71	0.79	3.43	3.52	2.02
Ca	2.21	1.74	1.64	0.57	1.40	0.27	0.33	0.34	0.79	0.80	0.81	1.89	1.83	0.00
Na	0.00	0.01	0.00	0.39	0.00	0.71	0.66	0.64	0.17	0.17	0.11	0.50	0.54	0.02
K	-	-	-	0.00	-	0.01	0.02	0.02	0.00	0.00	0.01	0.15	0.11	0.96
Cr	0.01	0.01	0.01	0.00	0.02	-	0.00	0.00	-	0.01	0.01	0.03	-	0.01
Alm	0.27	0.34	0.36		0.38									
Grs	0.37	0.29	0.28		0.23									
Py	0.36	0.36	0.35		0.38									
Jd				0.38					0.15	0.17	0.07			
Ab						0.72	0.66	0.64						
An						0.27	0.33	0.34						

Accepted Article

This article is protected by copyright. All rights reserved.

Table 3. Analyzed bulk composition and adjusted and calculated compositions used for phase equilibrium modelling, all in weight % of oxides.

	XRF-derived	Adjusted	Melt pocket	Symplectite
SiO_2	52.34	51.87	51.17	54.59
Al_2O_3	20.46	20.27	18.00	11.56
TiO_2	0.30	0.29	-	-
FeO_{TOT}	5.67	5.62	6.86	3.19
MnO	0.10	0.10	0.14	-
MgO	7.50	7.43	8.26	9.99
CaO	11.28	11.10	11.40	16.37
Na_2O	2.90	2.87	3.74	3.61
K_2O	0.12	0.12	-	0.19
O_2	-	0.03	0.04	-
P_2O_5	0.06	-	-	-
H_2O	-	0.30	0.40	0.50
Total	100.72	100.00	100.00	100.00

Accepted Article

This article is protected by copyright. All rights reserved.

Accepted Article

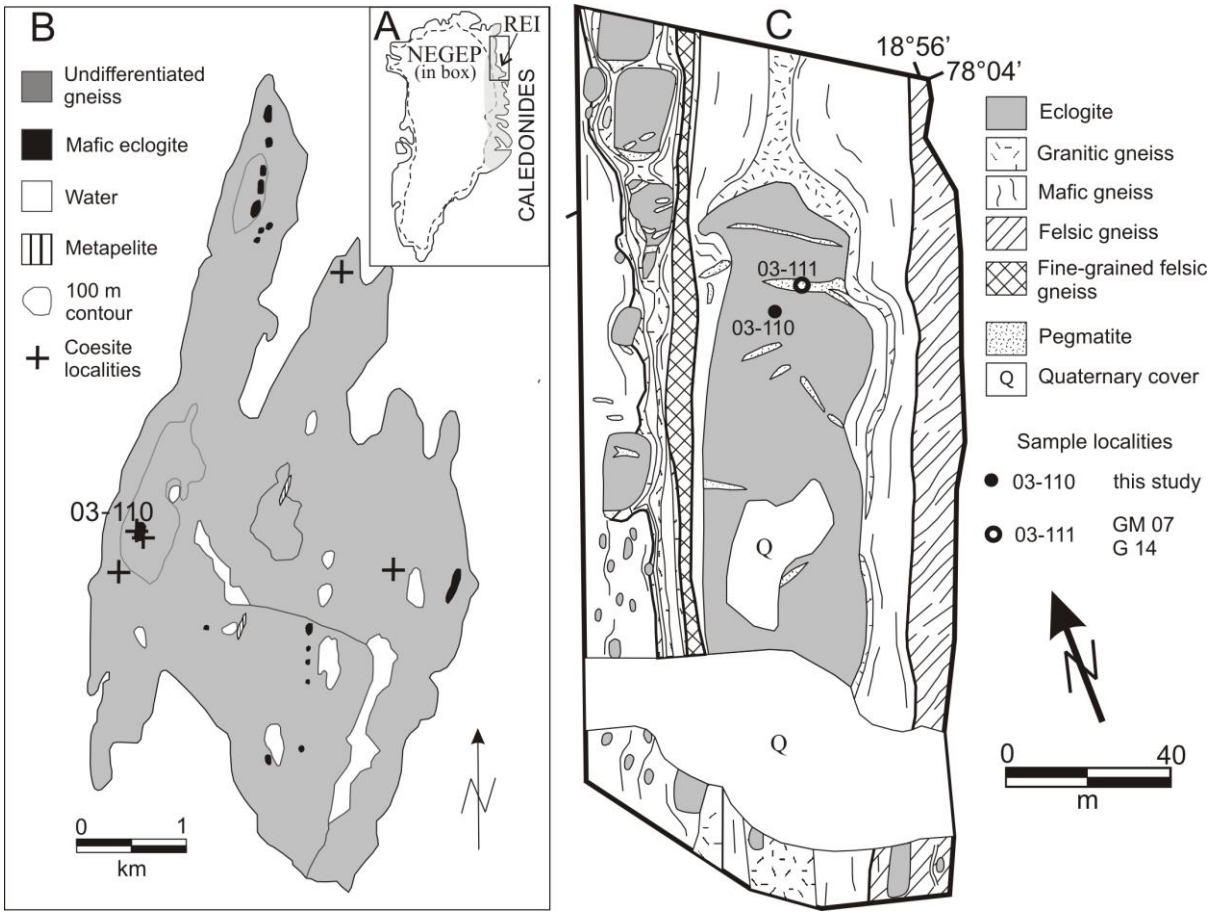

This article is protected by copyright. All rights reserved.

Accepted Article

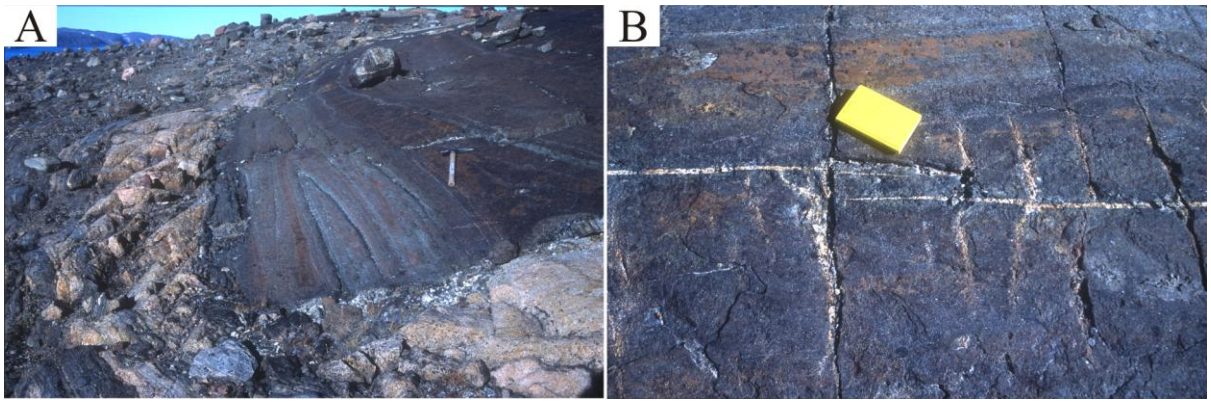

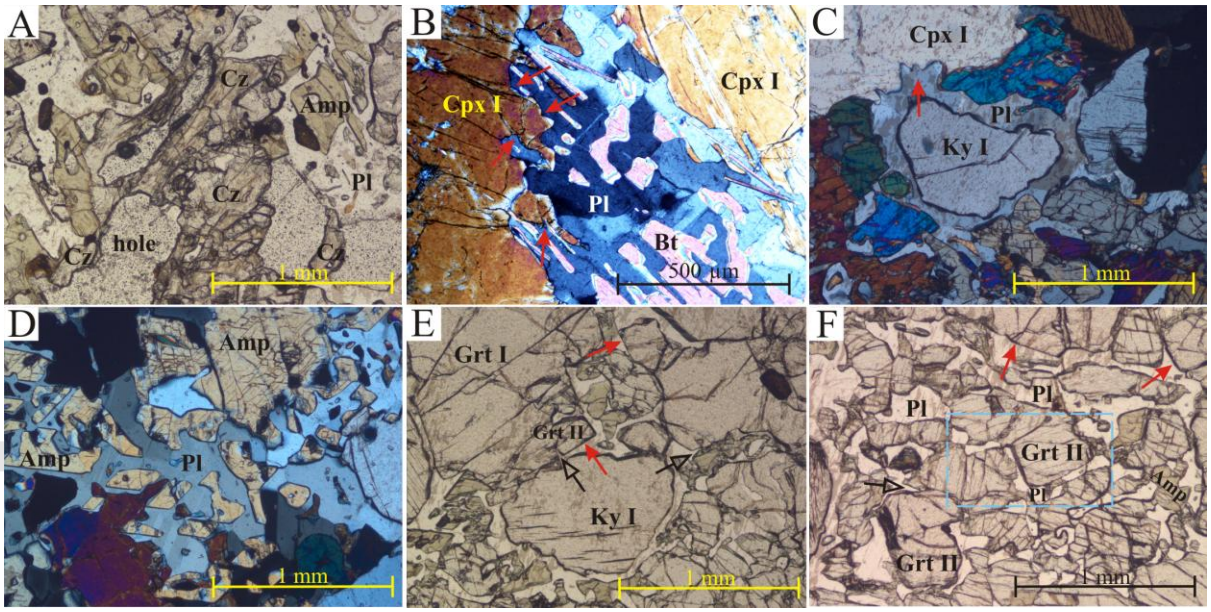

This article is protected by copyright. All rights reserved.

Accepted Article

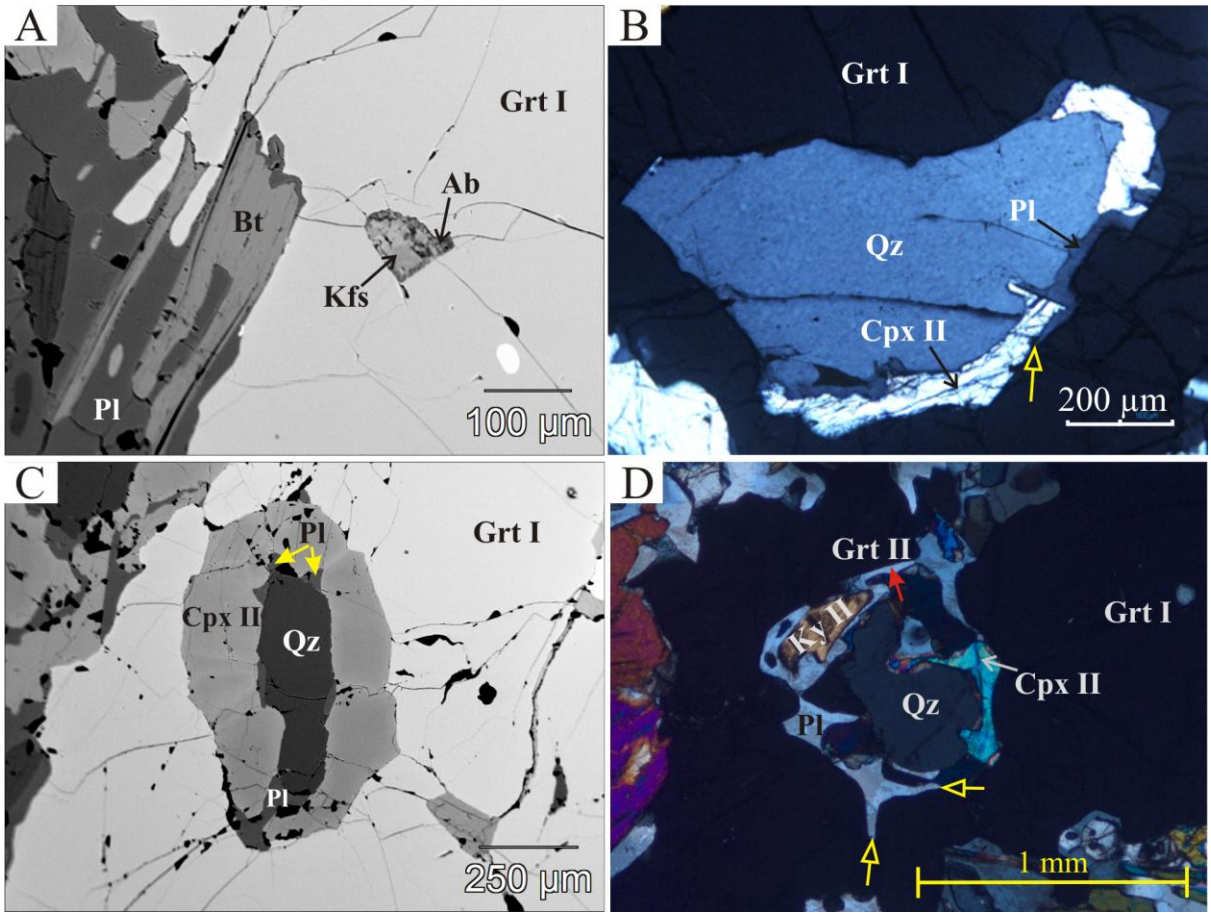

This article is protected by copyright. All rights reserved.

Accepted Article

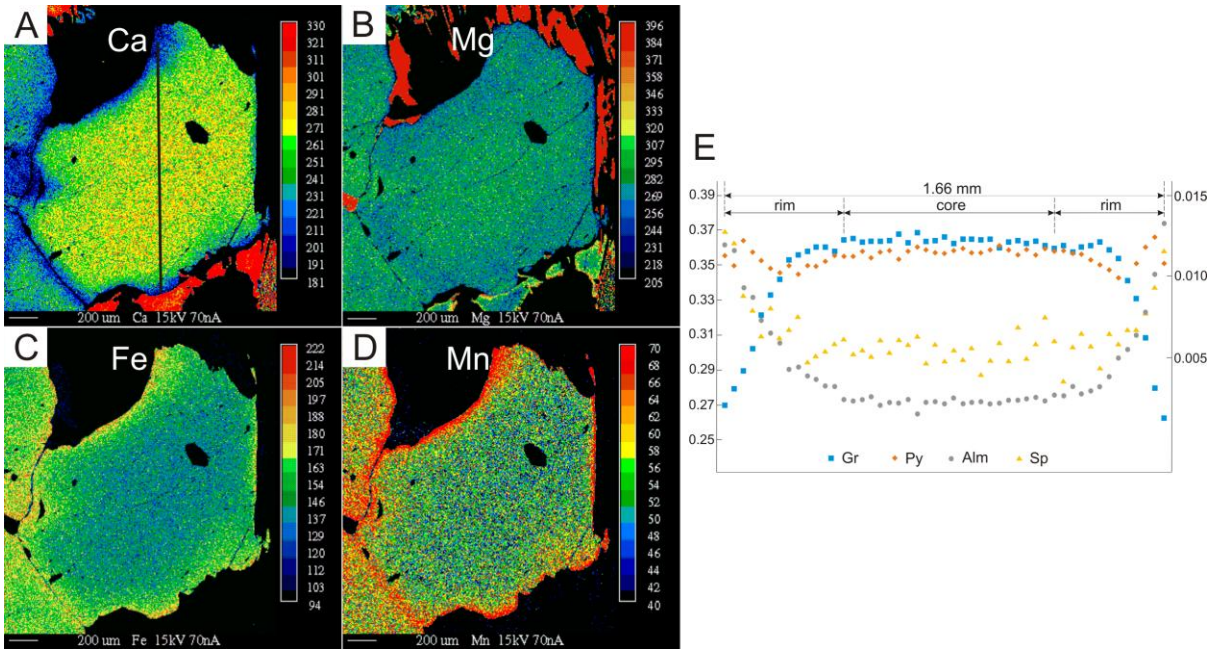

This article is protected by copyright. All rights reserved.

Accepted Article

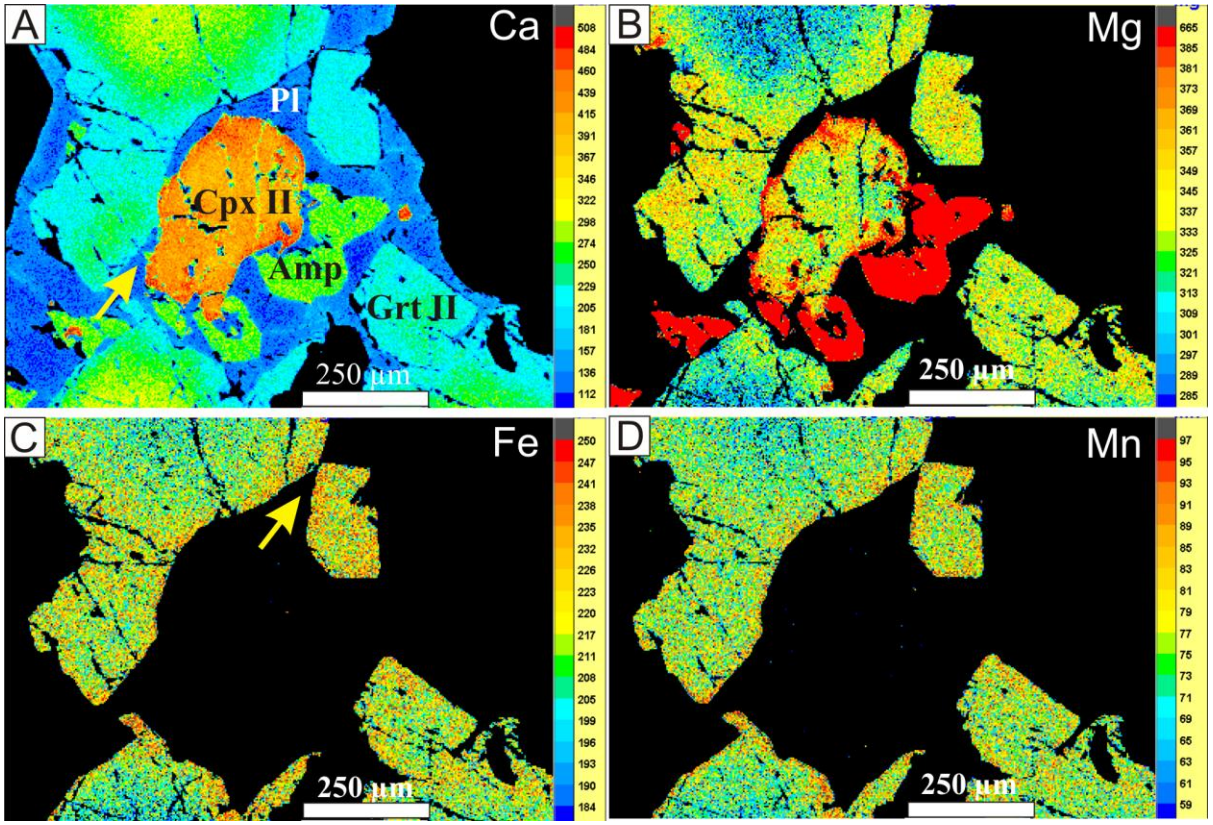

This article is protected by copyright. All rights reserved.

Accepted Article

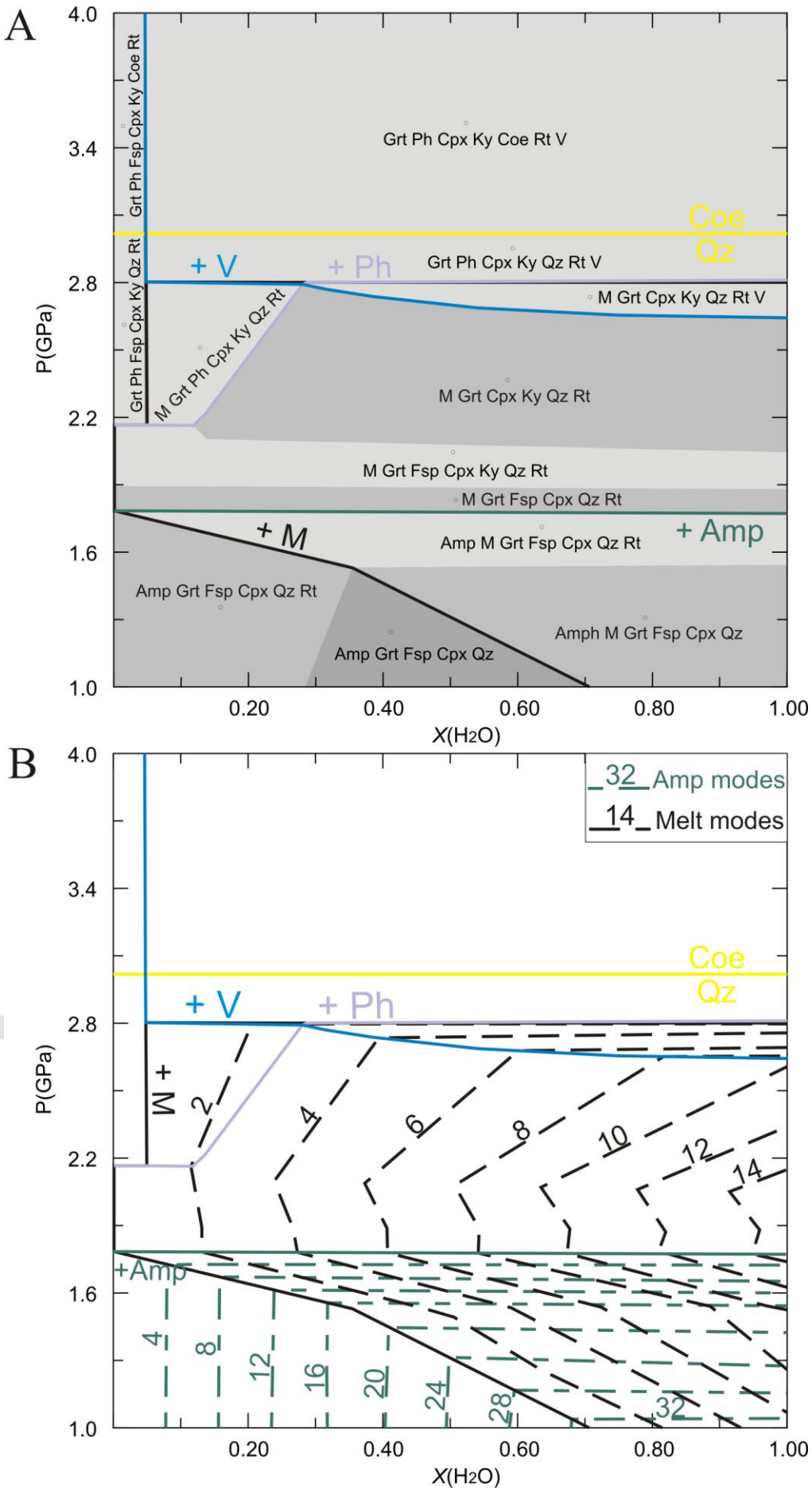

This article is protected by copyright. All rights reserved.

Accepted Article

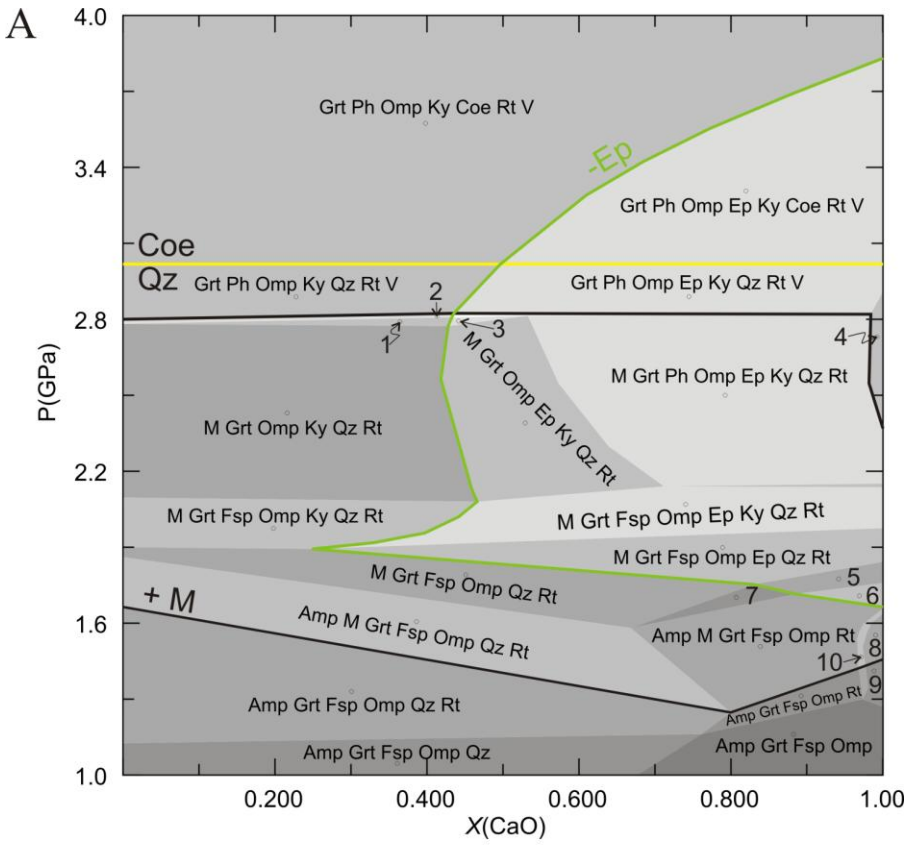

1 M Grt Omp Ky Qz Rt V
2 M Grt Ph Omp Ky Qz Rt V
3 M Grt Omp Ep Ky Qz Rt V
4 Grt Ph Omp Ep Ky Qz Rt
5 M Grt Fsp Omp Ep Rt
6 Amp M Grt Fsp Omp Ep Rt
7 M Grt Fsp Omp Rt
8 Amp M Grt Fsp Omp Tt
9 Amp Grt Fsp Omp Tt
10 Amp M Grt Fsp Omp Tt Rt

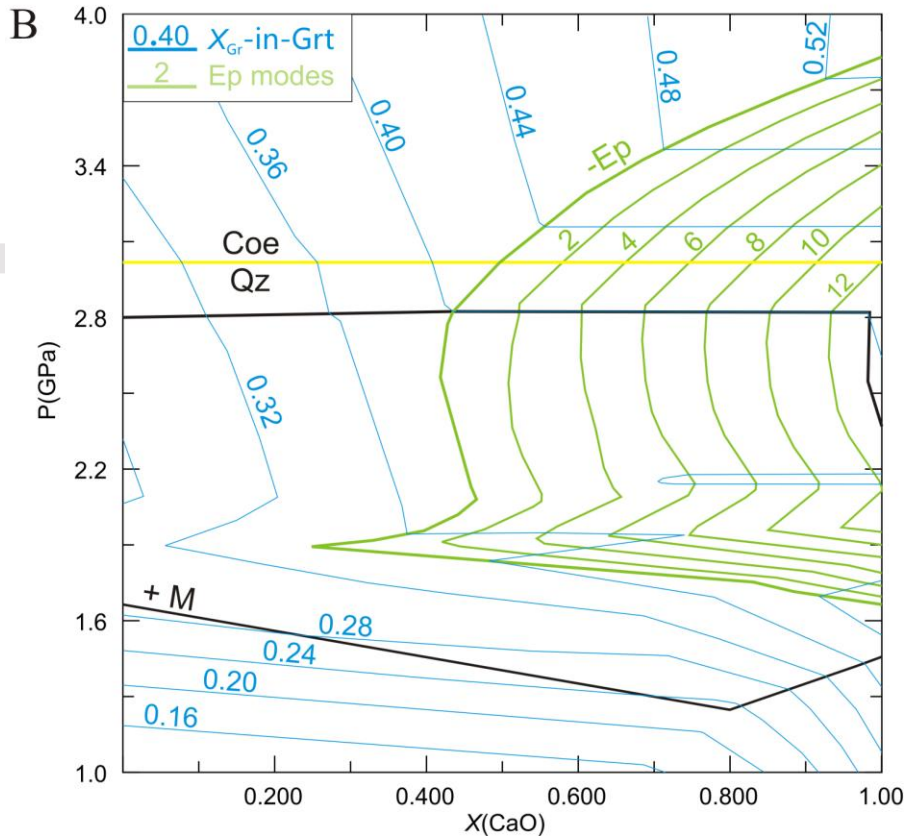

This article is protected by copyright. All rights reserved.

Accepted Article

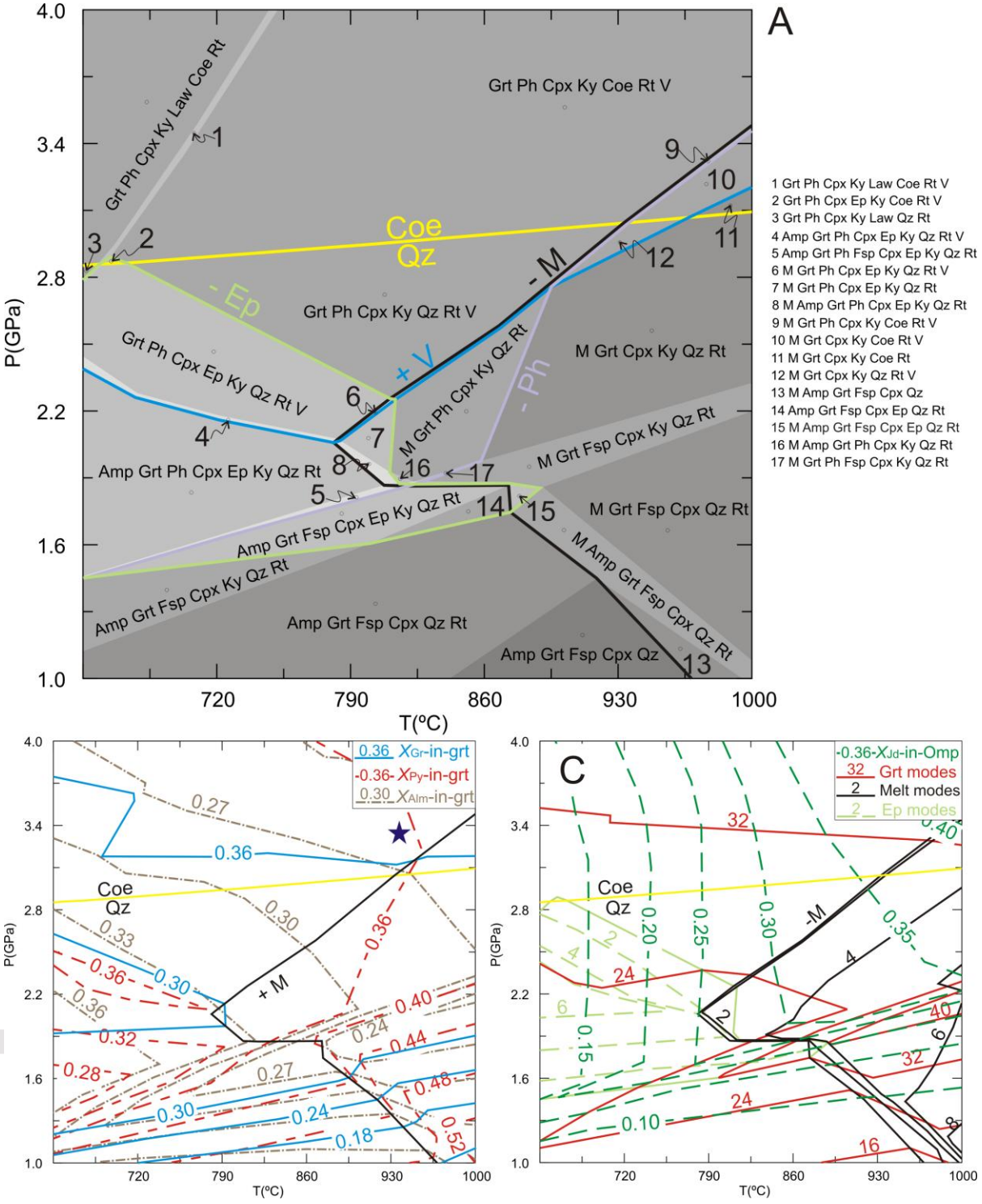

This article is protected by copyright. All rights reserved.

Accepted Article

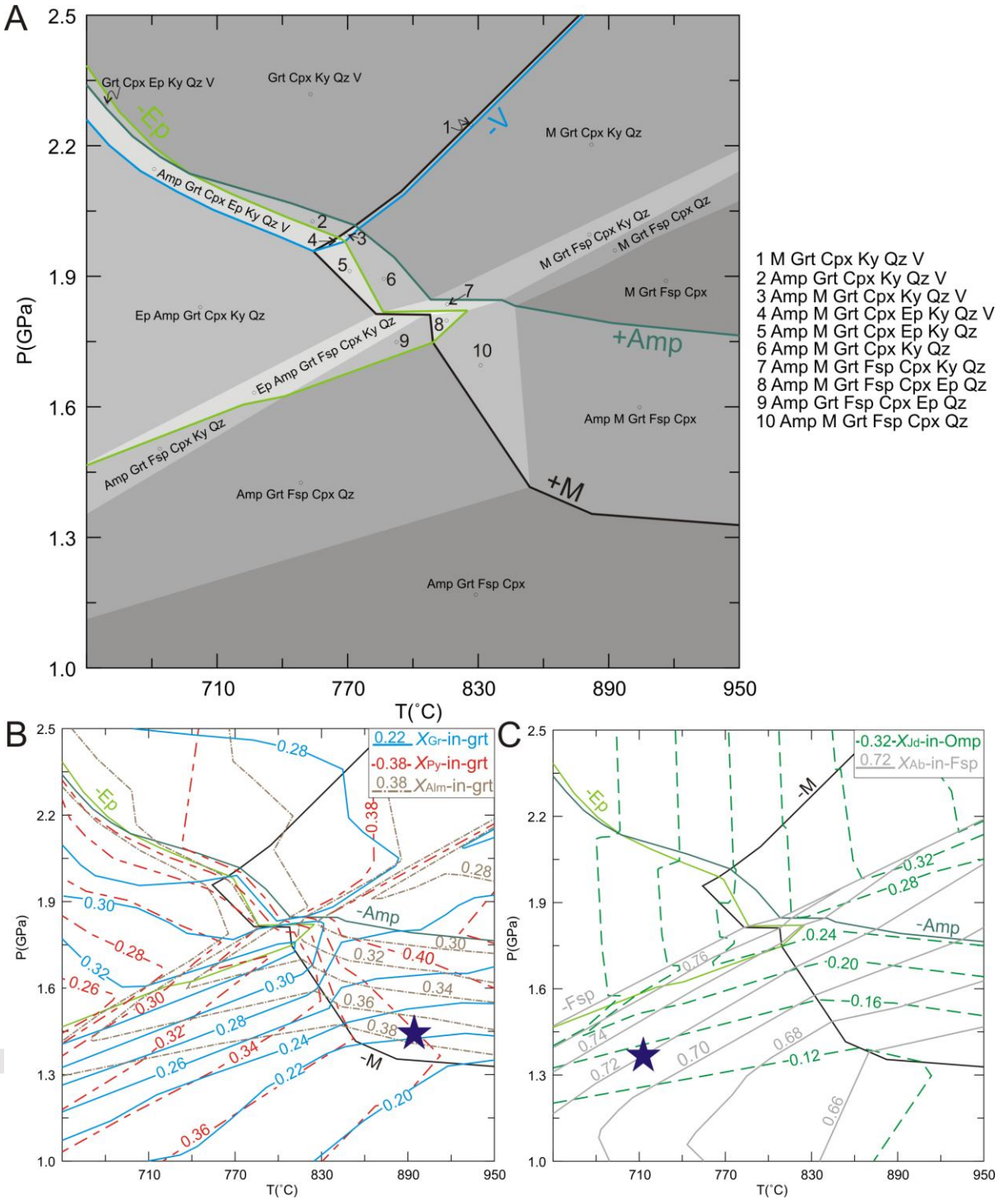

This article is protected by copyright. All rights reserved.

Accepted Article

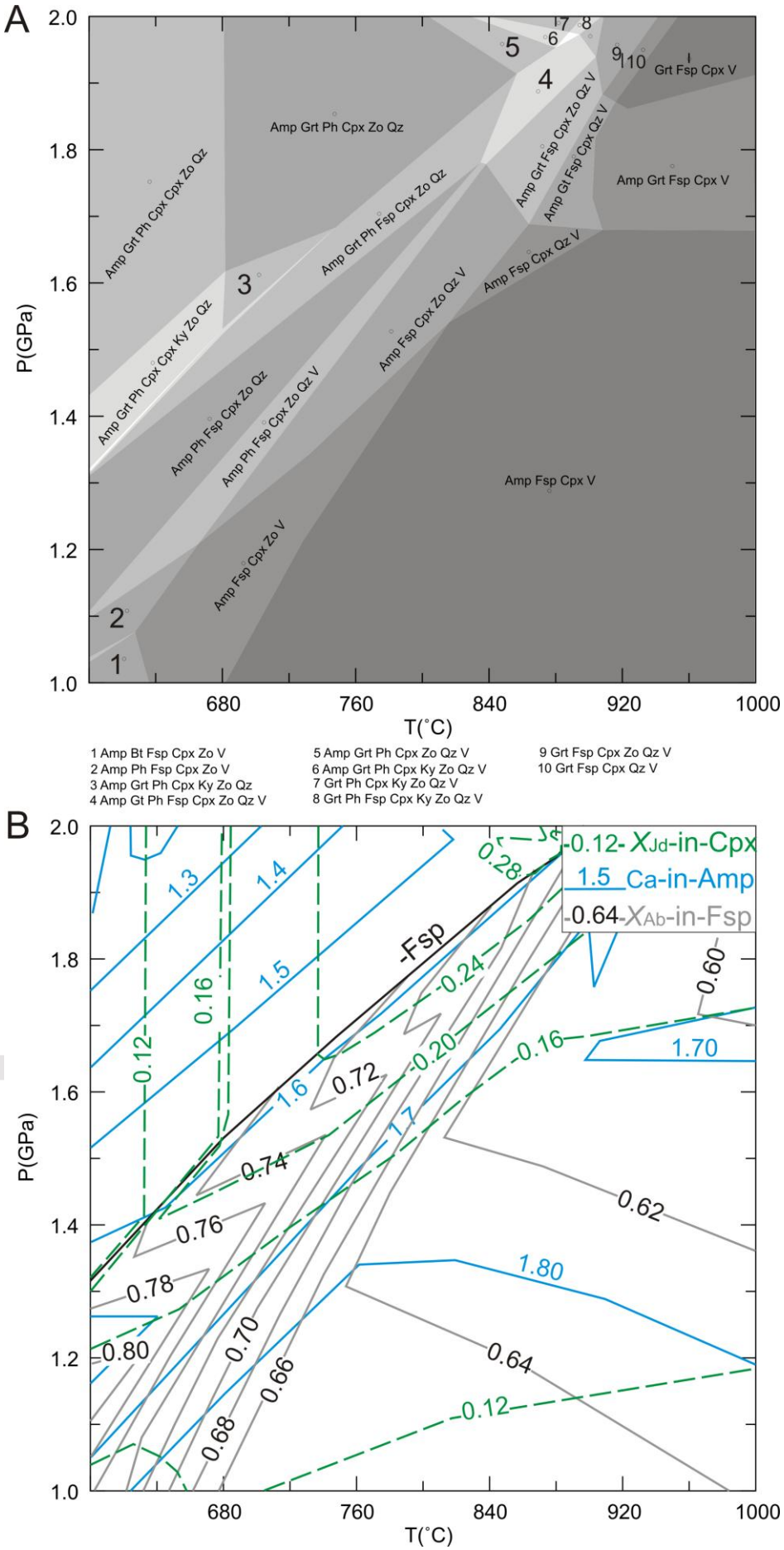

This article is protected by copyright. All rights reserved.

Accepted Article

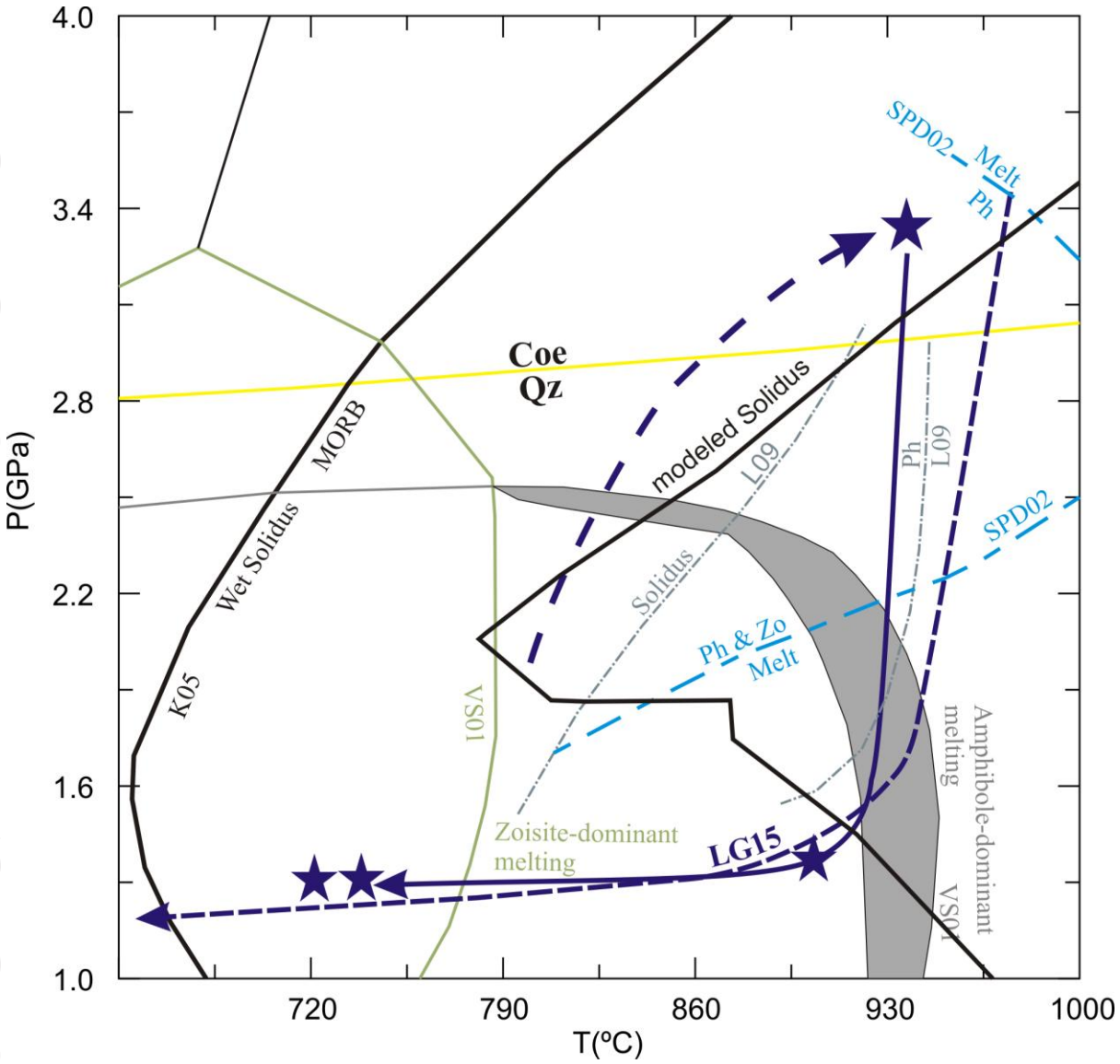

This article is protected by copyright. All rights reserved.